Electronic Supplementary Material (ESI) for Physical Chemistry Chemical Physics.

Electronic supplementary information

# Synchrotron-based Mössbauer Spectroscopy Characterization of Sublimated Spin Crossover Molecules

Alberto Cini,[a] Lorenzo Poggini,[b] Alexander I. Chumakov,[c] Rudolf Rüffer,[c] Gabriele Spina,[a] Alain Wattiaux,[b] Mathieu Duttine,[b] Mathieu Gonidec,[b] Maria Fittipaldi,*[a] Patrick Rosa*[b] and Matteo Mannini*[d]

[a] Department of Physics and Astronomy, University of Florence and INSTM Research Unit of Florence, via Sansone 1, I-50019 Sesto Fiorentino (FI), Italy.

E-mail: maria.fittipaldi@unifi.it

[b] CNRS, Univ. Bordeaux, Bordeaux INP, ICMCB, UMR 5026, F-33600 Pessac, France.

E-mail: patrick.rosa@icmcb.cnrs.fr

[c] ESRF-The European Synchrotron, 71, Avenue des Martyrs, Grenoble, France.

[d] Department of Chemistry "Ugo Schiff", University of Florence and INSTM Research Unit of Florence, via della Lastruccia 3-13, I-50019 Sesto Fiorentino (FI), Italy.

E-mail: matteo.mannini@unifi.it

## S1. Supplementary figures

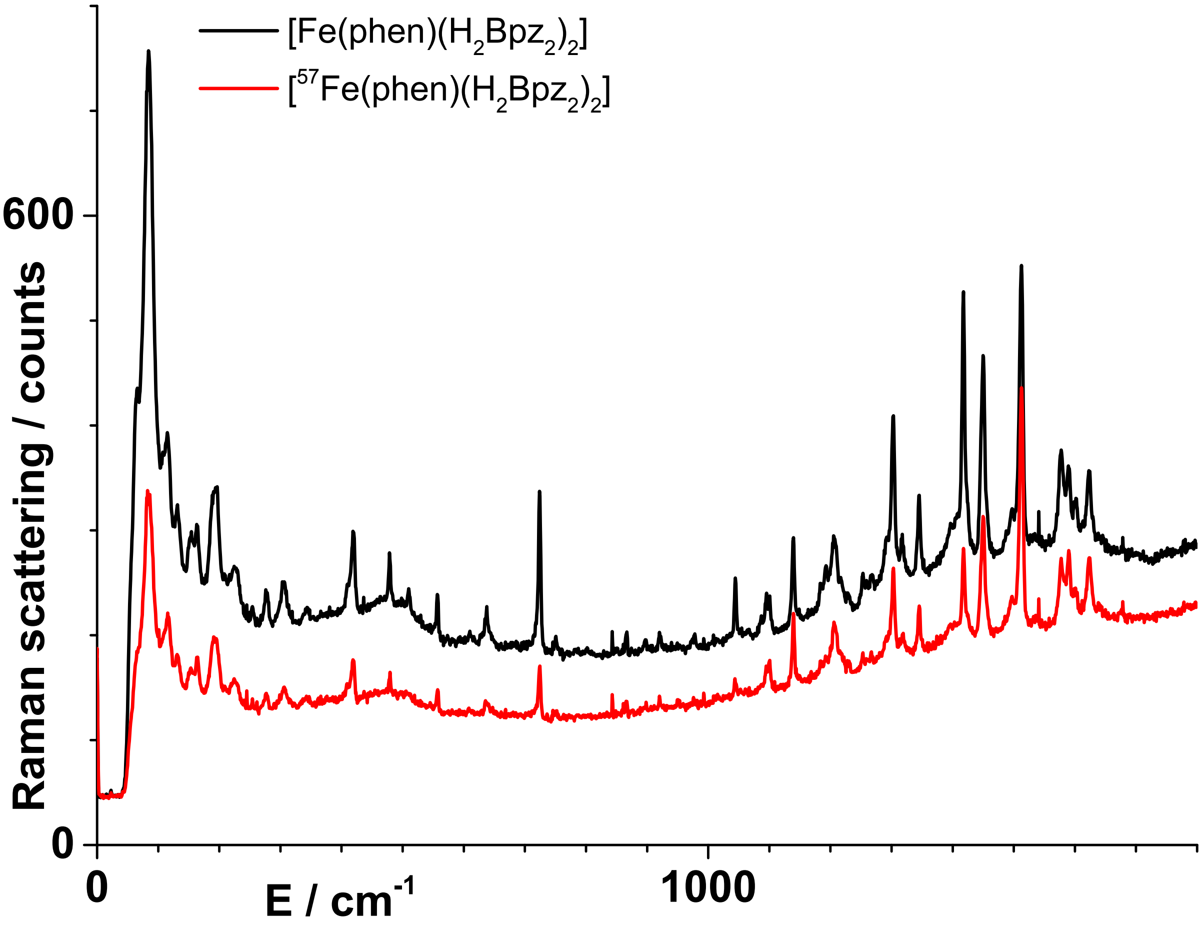

***Figure S1.*** *Comparison of Raman spectra at room temperature (300 K) for bulk **1**: natural abundance $^{57}$Fe (black line) and $^{57}$Fe enriched material (red line).*

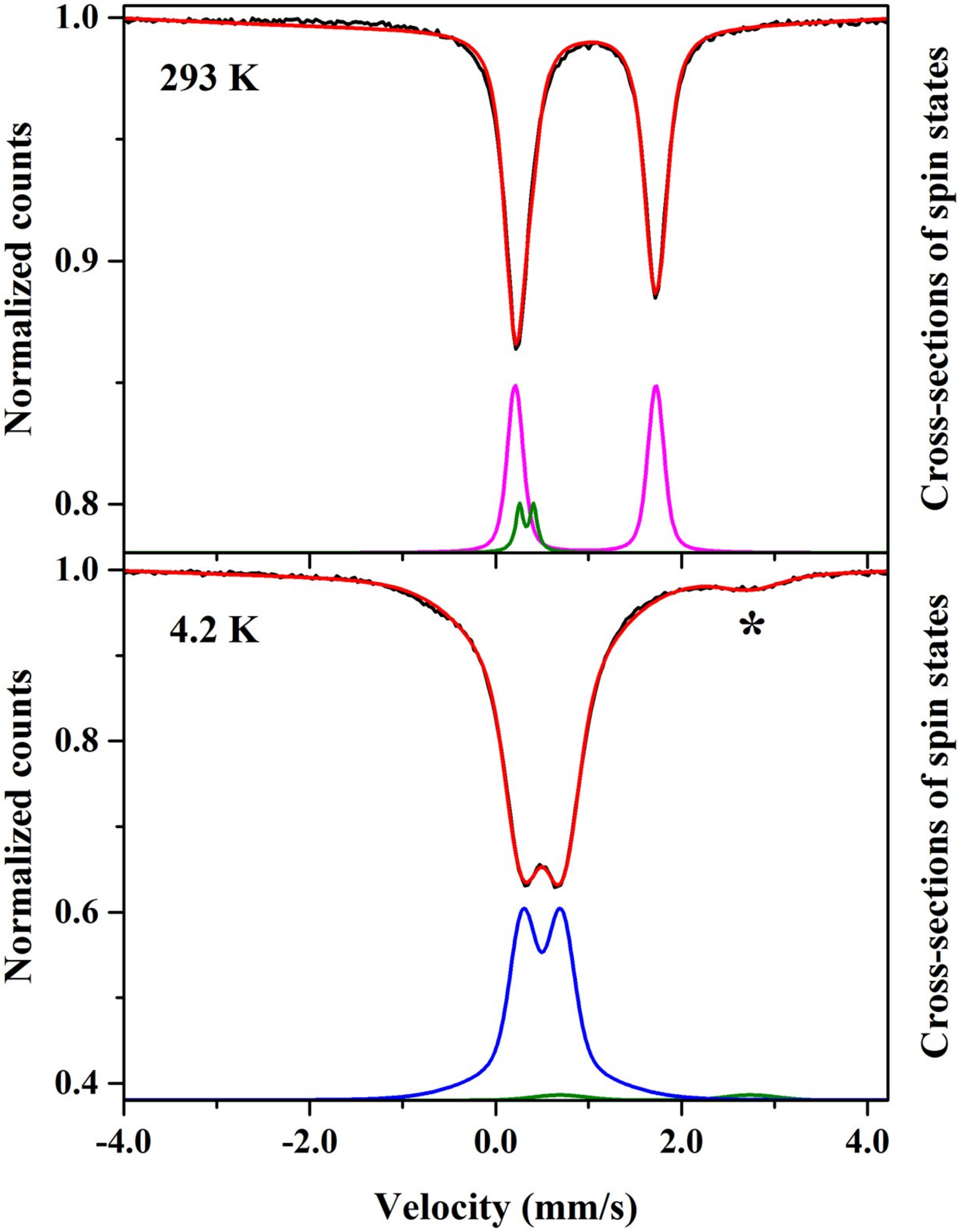

***Figure S2.*** *$^{57}$Fe Mössbauer spectra of the powder sample realized with a standard setup (black lines) and corresponding best fit curves (red lines) The absorption cross-sections associated to the HS state (magenta line) and the LS state (blue line) together with a minor impurity present at both temperatures (green line) are shown. The asterisk in the bottom panel underlines the contribution of the impurity to the Mössbauer spectrum of the sample.*

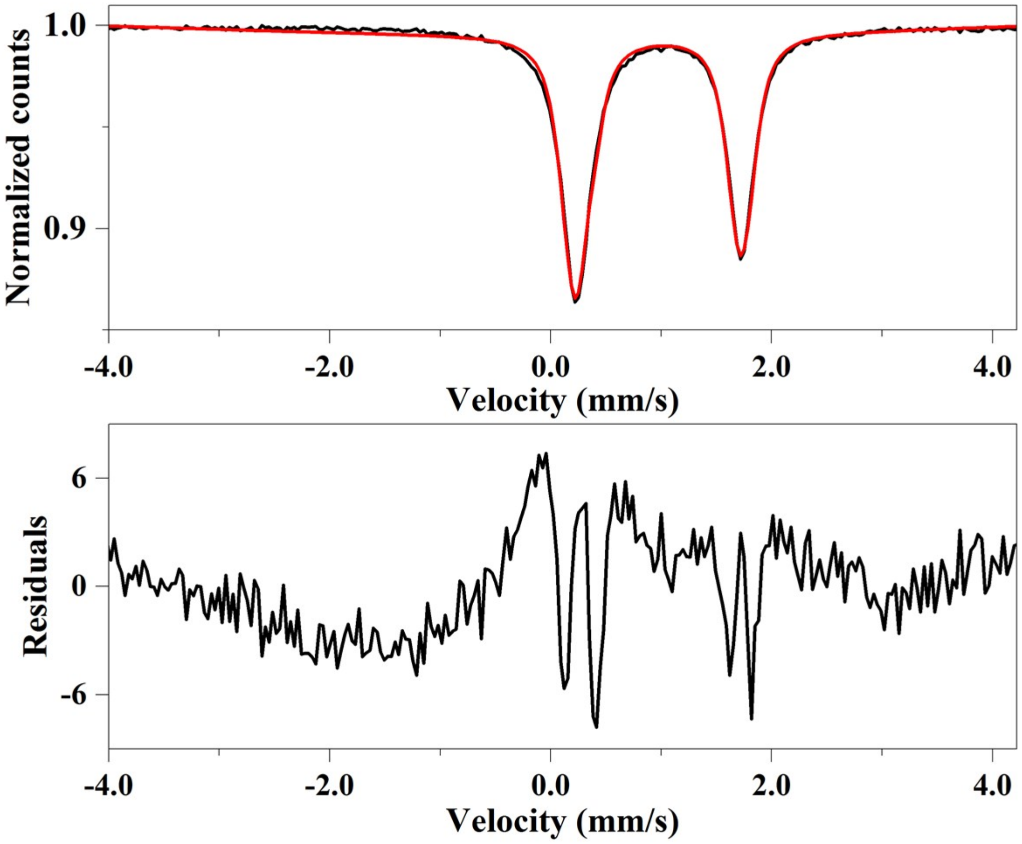

***Figure S3.*** *Top panel:* $^{57}$*Fe Mössbauer spectrum of a powder sample of* $^{57}$***1*** *at 293 K (measured spectrum in black and relative fit in red). Bottom panel: residuals of the fitting procedure.*

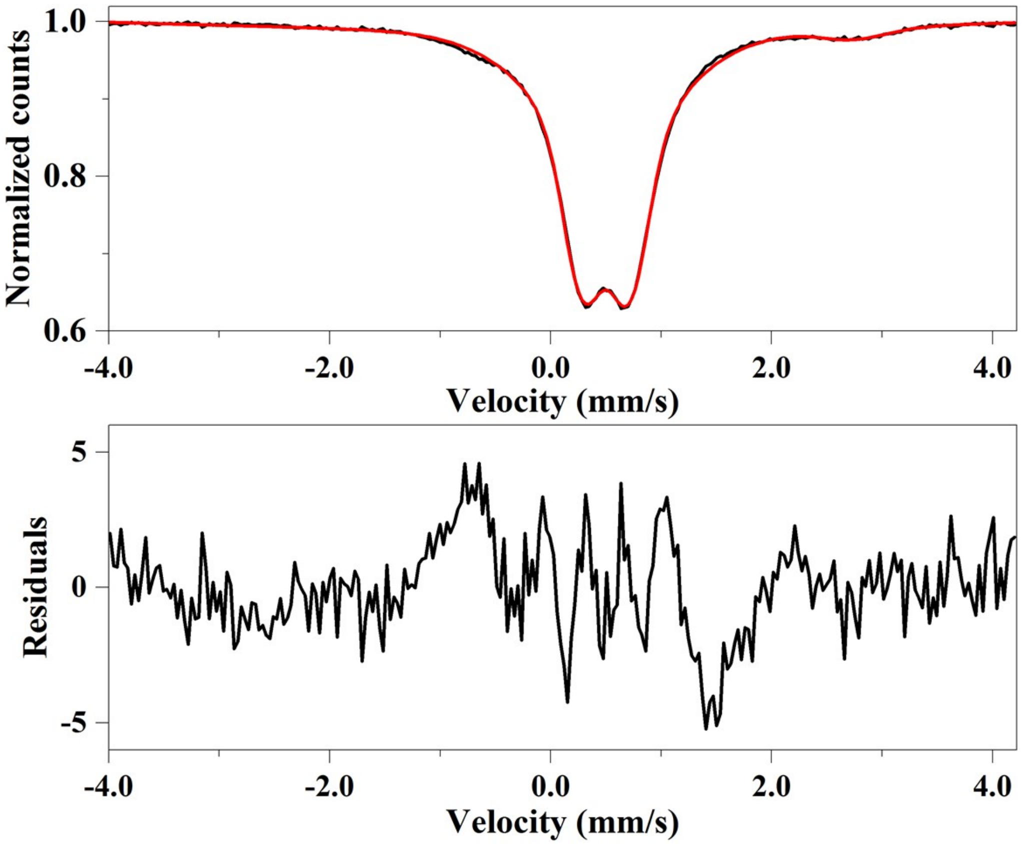

***Figure S4.*** *Top panel:* $^{57}$*Fe Mössbauer spectrum of a powder sample of* $^{57}$***1*** *at 4.2 K (measured spectrum in black and relative fit in red). Bottom panel: residuals of the fitting procedure.*

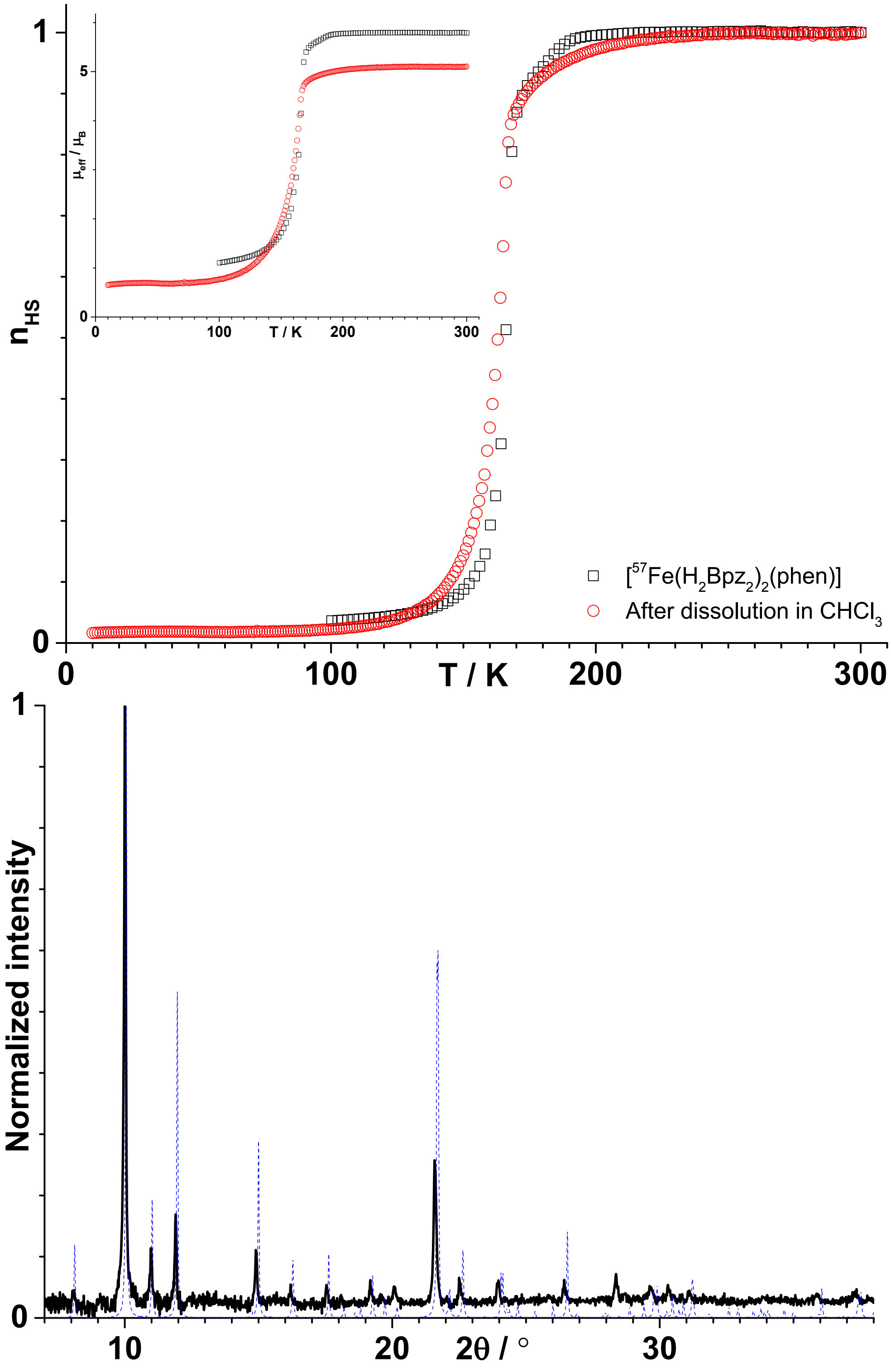

***Figure S5.*** *(top) High-spin Fe(II) thermal distribution profile obtained by standard magnetometry taken before (red empty circles) and after (black empty squares) dissolution in* $CHCl_3$*, with* $T_{1/2}$ *= 159±2 K and* $T_{1/2}$ *= 163 ± 2 K respectively. (inset) corresponding effective magnetic moment dependence with T. The 300 K values were used as normalization factors to obtain the profile, neglecting the small residual LS fraction at that temperature. (bottom) Powder diffractogram of a* $CH_2Cl_2$ *dropcast of* $^{57}$***1*** *at RT (black line) compared to the pattern predicted from crystal structure NEFSUM01 (200 K, dotted blue line). Background was subtracted and both curves normalized to facilitate comparison.*

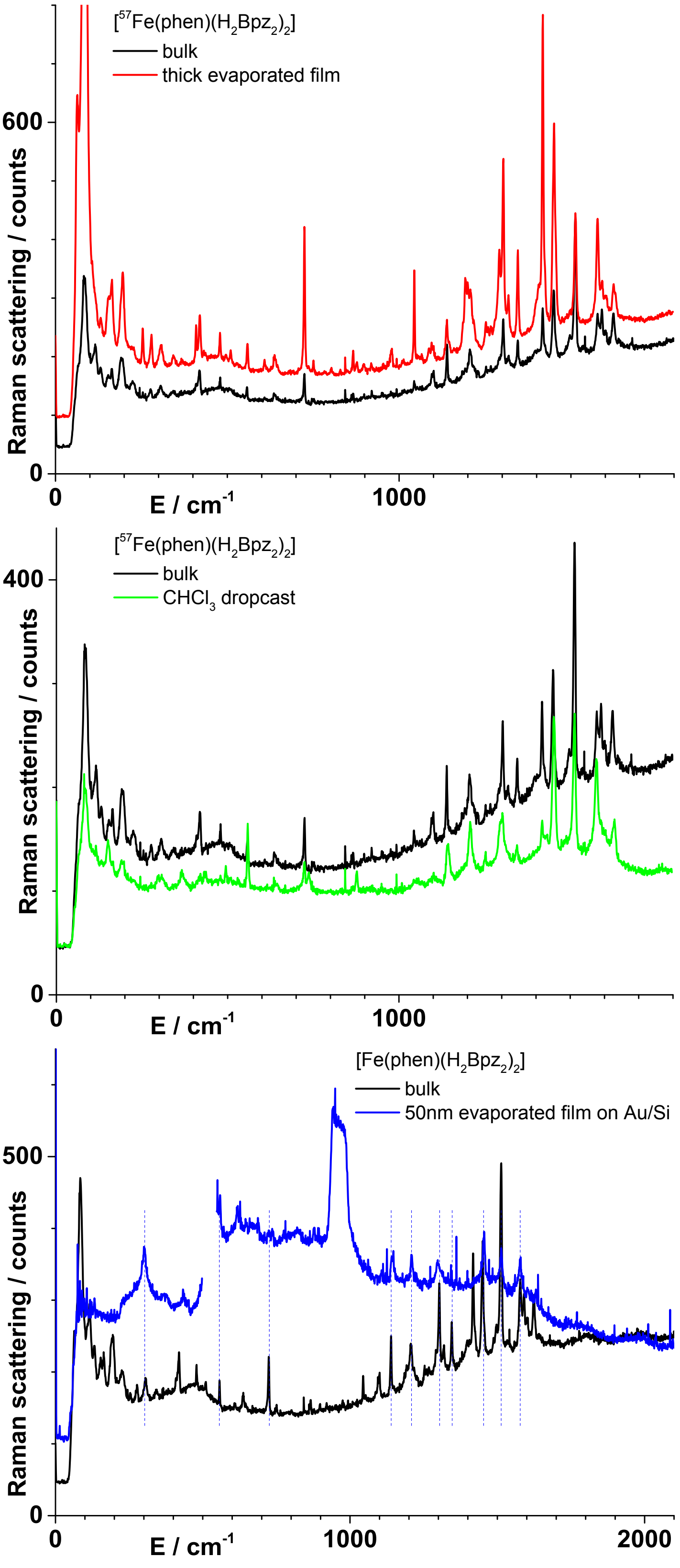

***Figure S6.*** *Comparison of Raman spectra at room temperature (300 K) for (top) $^{57}$Fe enriched bulk material $^{57}$**1** (black line) and a thick evaporated film of the same (red line); (middle) bulk $^{57}$**1** (black line) and the solid obtained after drying a $CHCl_3$ solution of the same (green line); (bottom) natural abundance bulk **1** (black line) and a 50 nm thick film of the same material evaporated on Au over Si (blue line). Note that $CHCl_3$ was used instead of $CH_2Cl_2$ since solubility of **1** in the latter is low.*

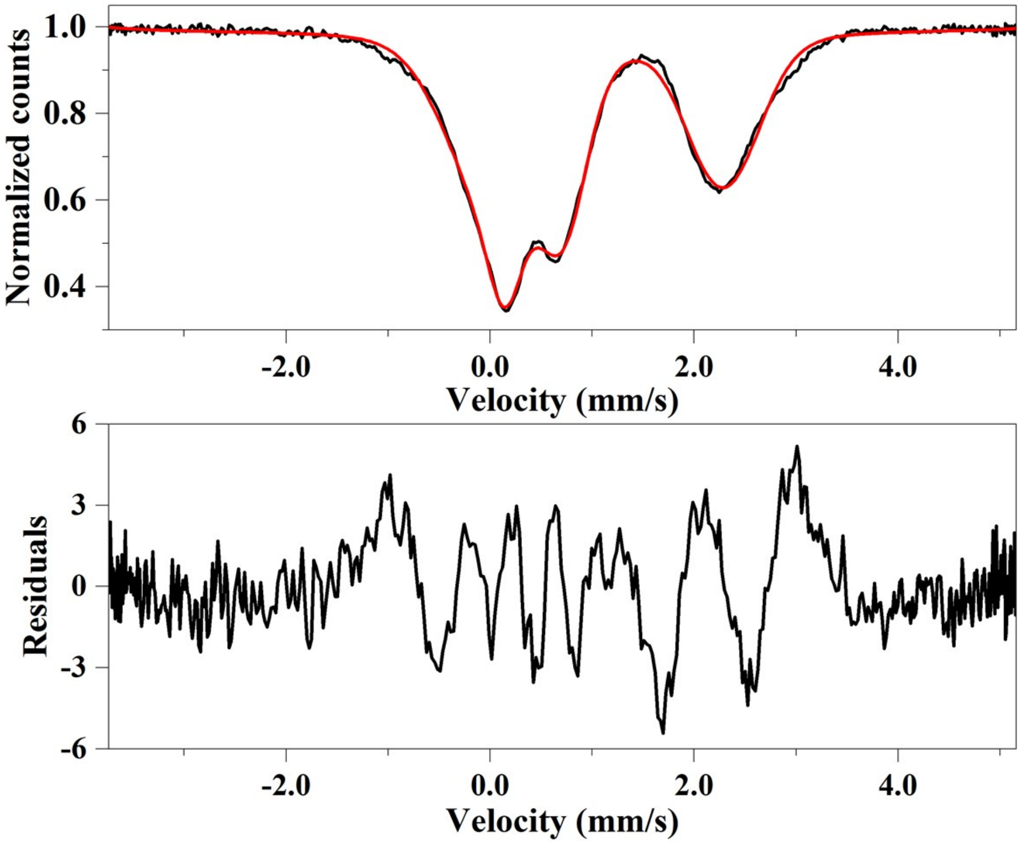

***Figure S7.*** *Top panel: SMS spectrum of the 50 nm thick sublimated sample at 3.0 K (measured spectrum in black and relative fit in red). Bottom panel: residuals of the fitting procedure.*

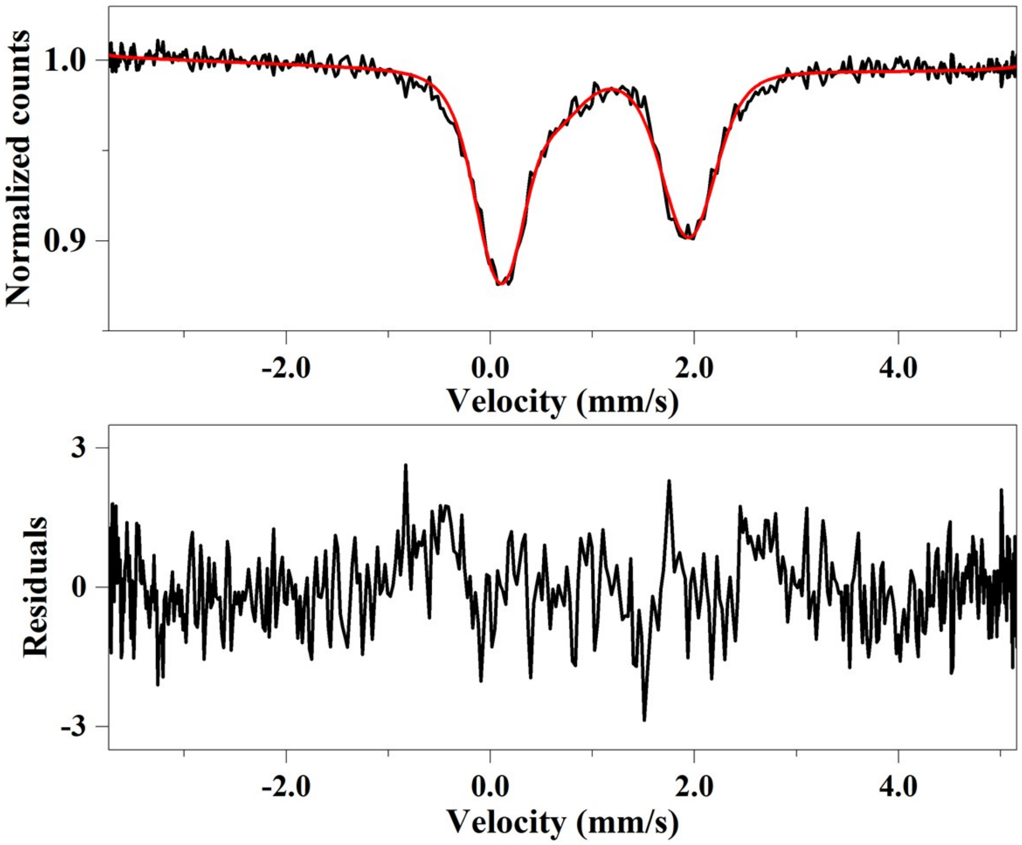

***Figure S8.*** *Top panel: SMS spectrum of the 50 nm thick sublimated sample at 240 K (measured spectrum in black and relative fit in red). Bottom panel: residuals of the fitting procedure.*

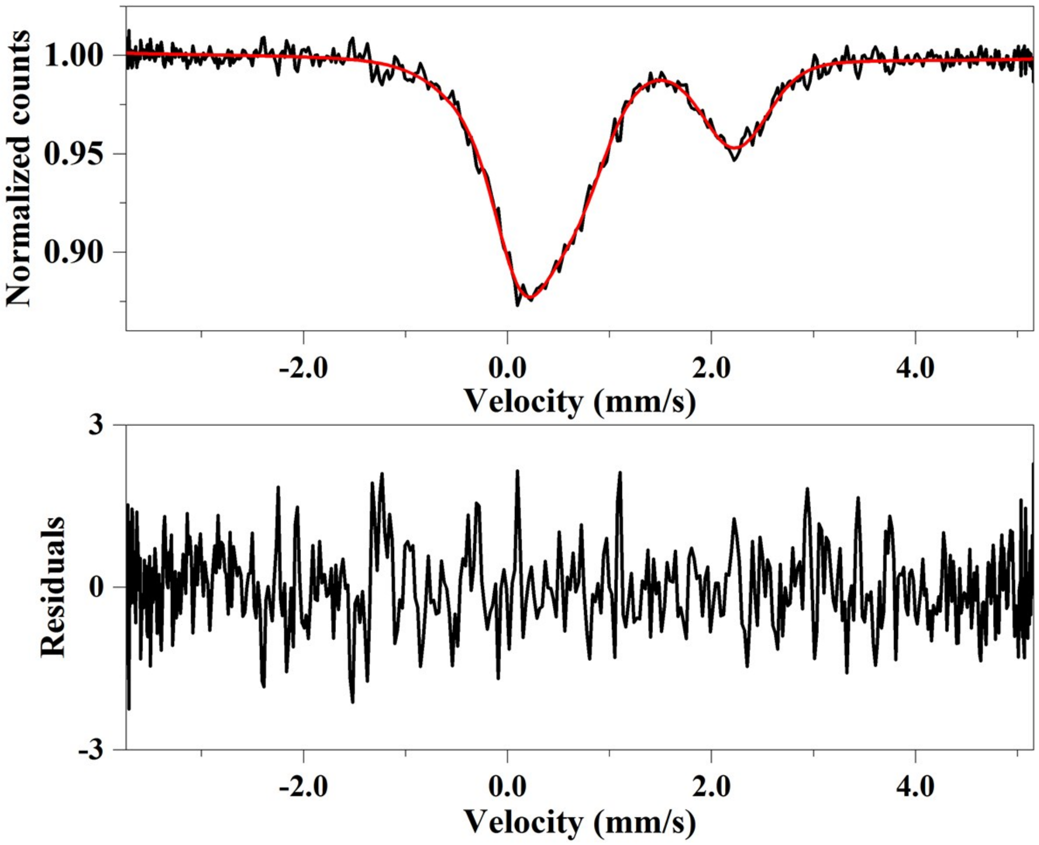

***Figure S9.*** *Top panel: SMS spectrum of the 5 nm thick sublimated sample at 3.0 K (measured spectrum in black and relative fit in red). Bottom panel: residuals of the fitting procedure.*

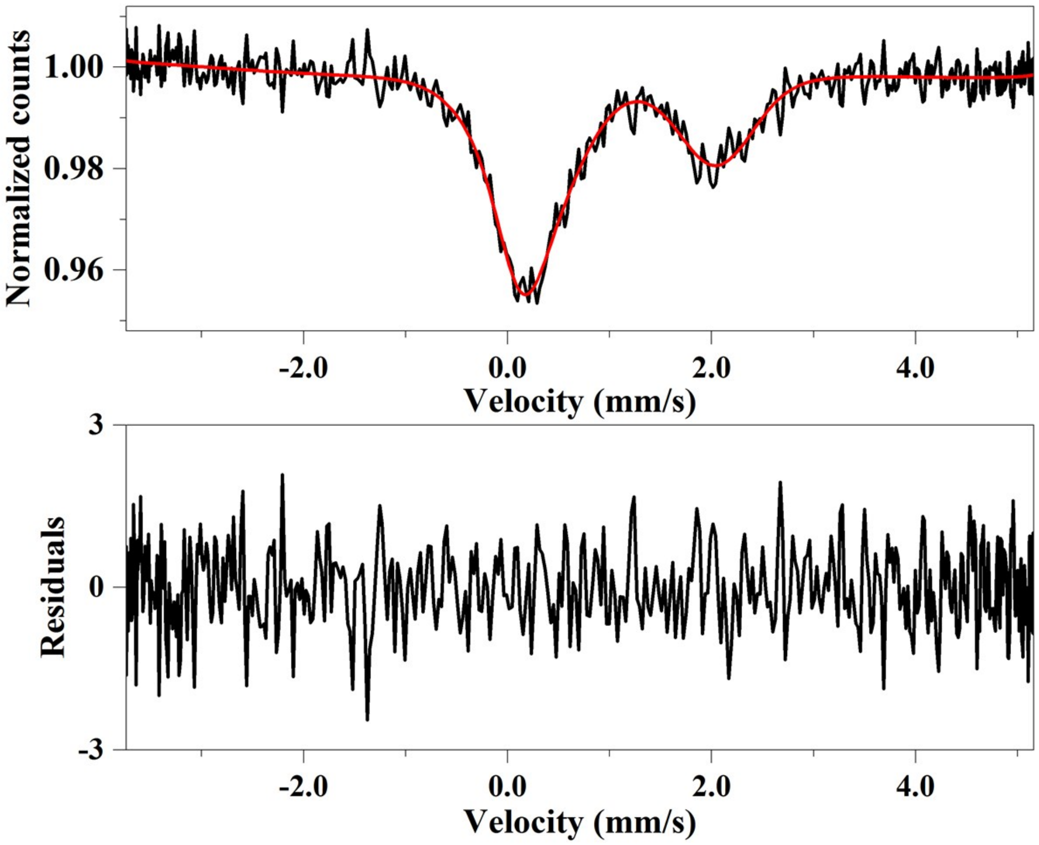

***Figure S10.*** *Top panel: SMS spectrum of the 5 nm thick sublimated sample at 177 K (measured spectrum in black and relative fit in red). Bottom panel: residuals of the fitting procedure.*

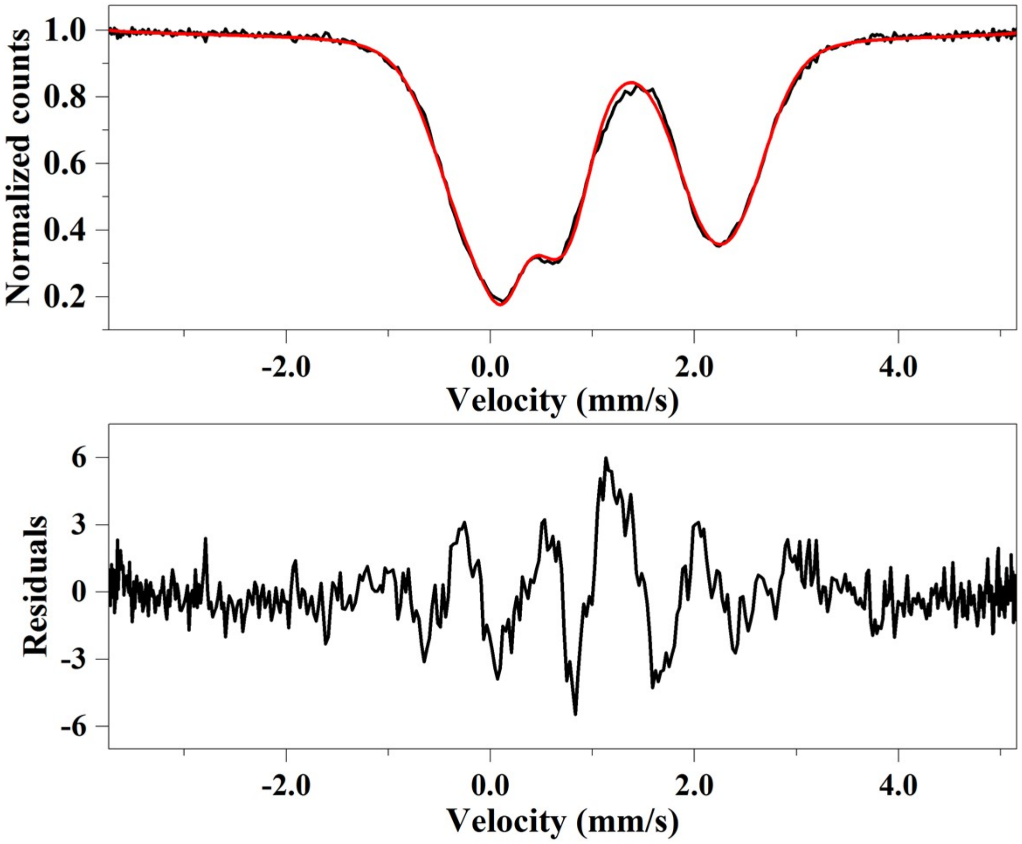

***Figure S11.*** *Top panel: SMS spectrum of the dropcast sample at 3.0 K (measured spectrum in black and relative fit in red). Bottom panel: residuals of the fitting procedure.*

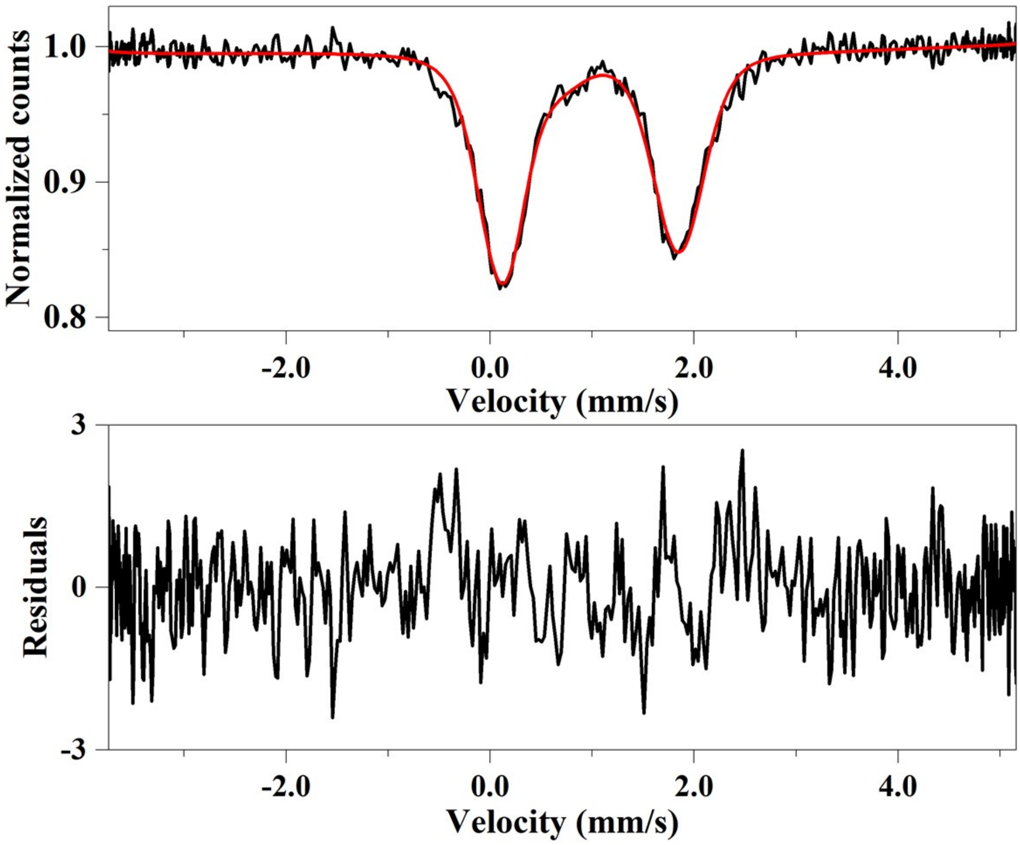

***Figure S12.*** *Top panel: SMS spectrum of the dropcast sample at 278 K (measured spectrum in black and relative fit in red). Bottom panel: residuals of the fitting procedure.*

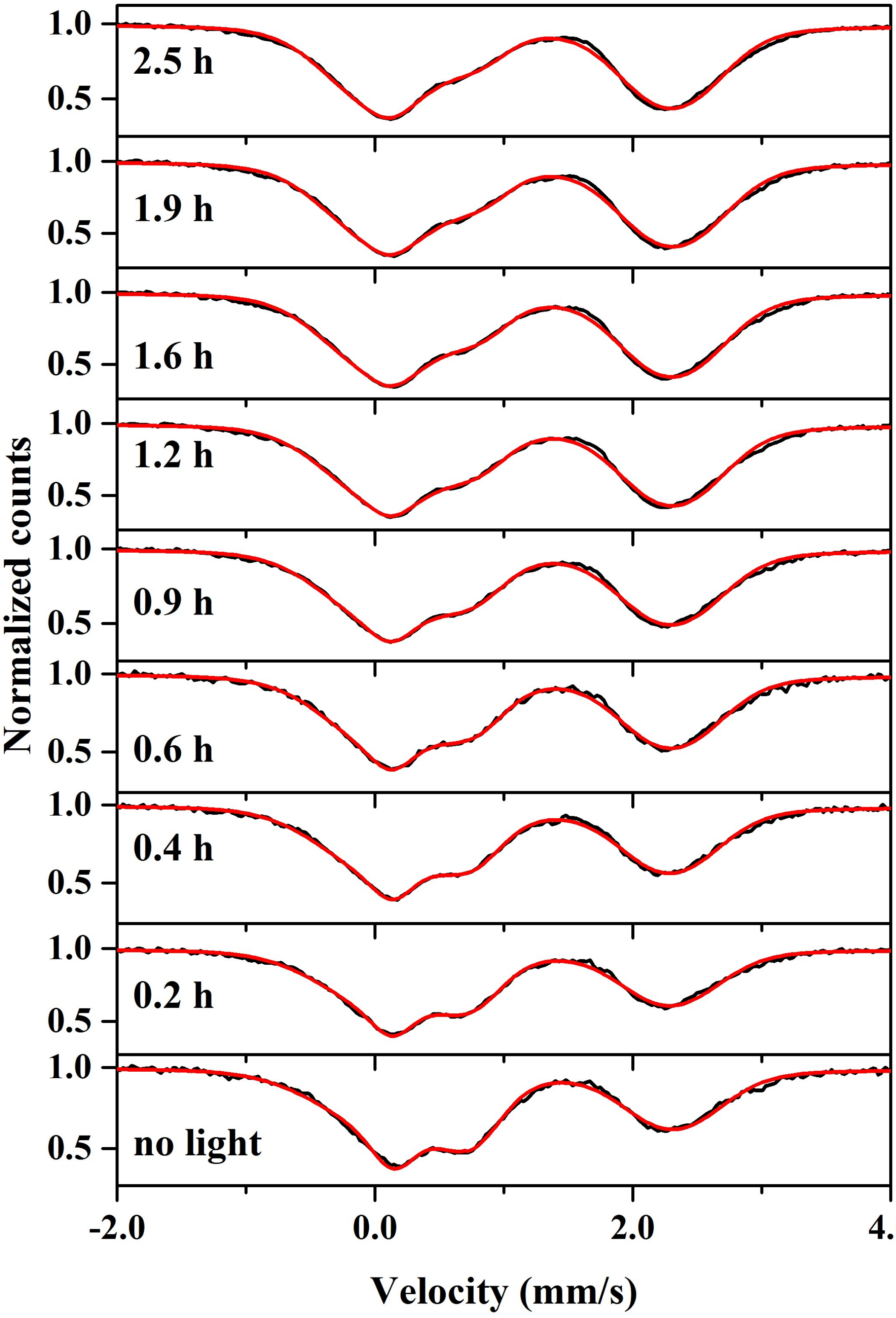

***Figure S13.*** *SMS spectra of the 50 nm thick sublimated sample at 6.0 K as a function of the irradiation time (measured spectrum in black and relative fit in red).*

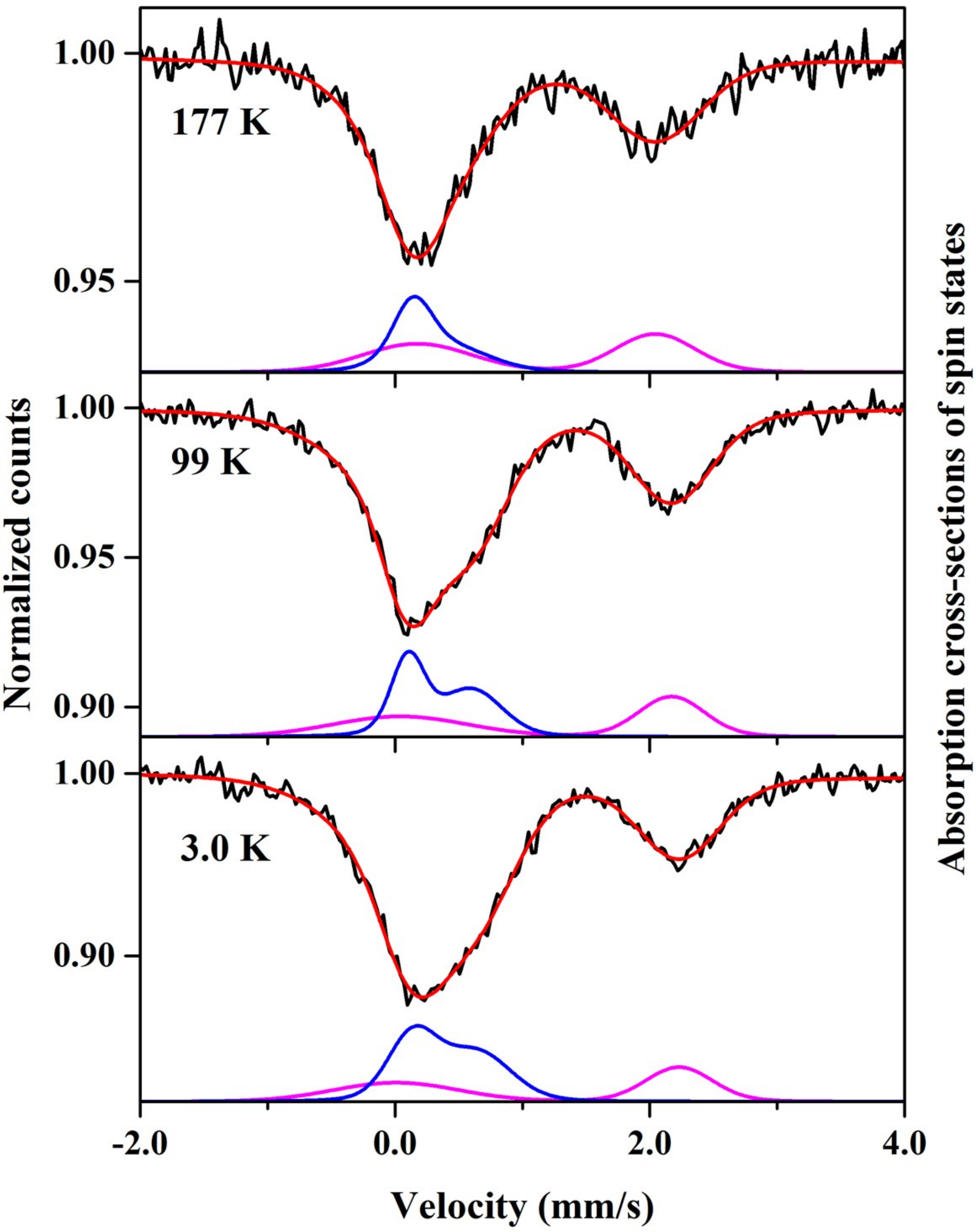

***Figure S14.*** *Experimental spectra (black lines) and best fit curves (red lines) of the 5 nm thick sublimated sample for three selected temperatures. The absorption cross-sections associated to the HS state (magenta line) and the LS state (blue line) are also shown. The velocity range is restricted to values showing a transmission different from unity.*

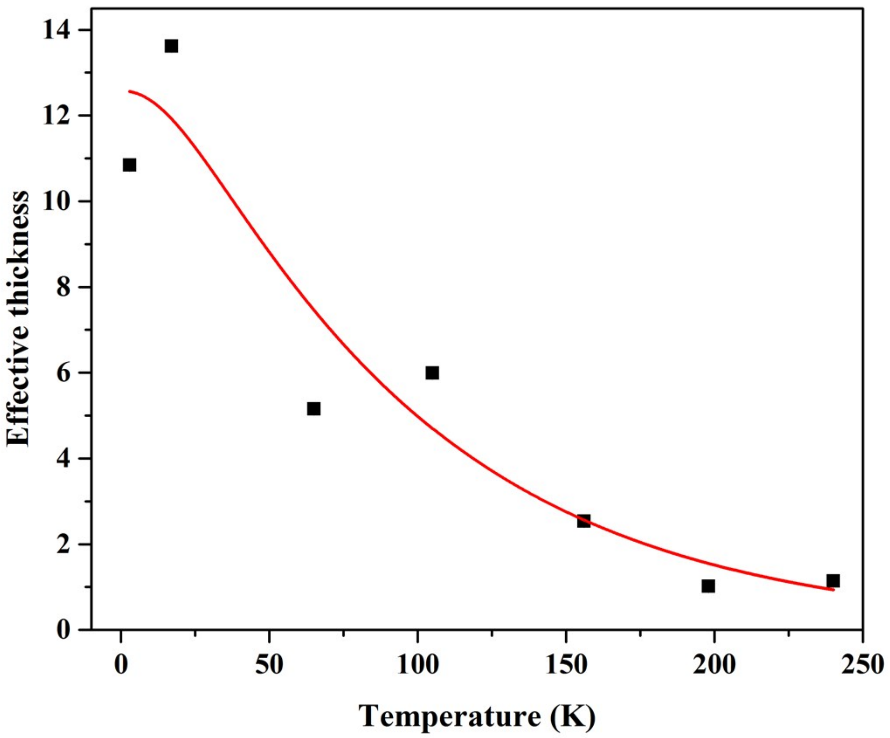

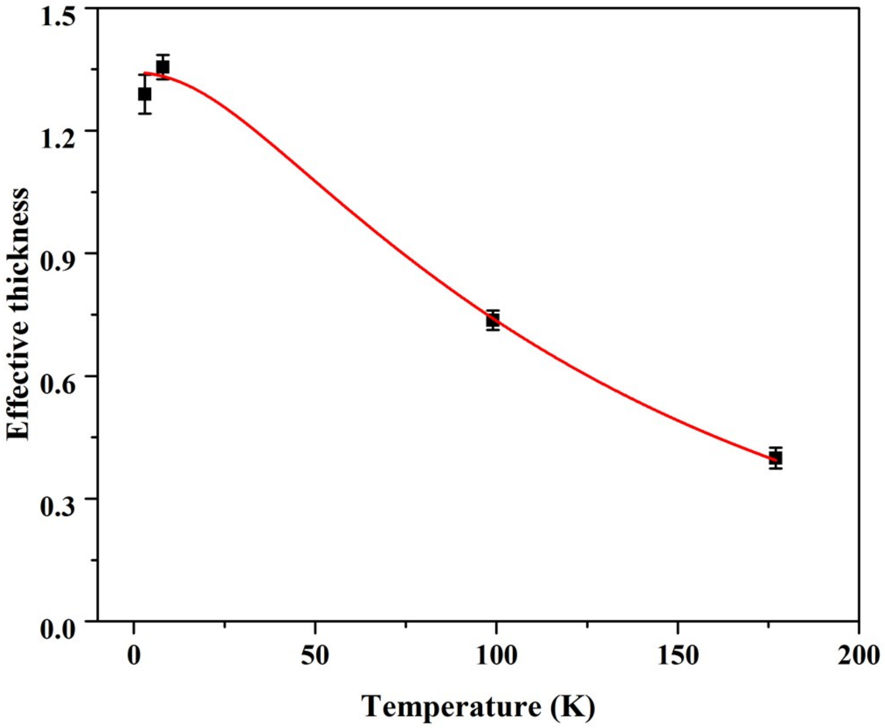

***Figure S15.*** *Effective thickness of the 50 nm (top) and 5 nm (bottom) thick sublimated samples extracted from the fit of the Mössbauer spectra in function of the temperature. The red line is the fit with the Debye model.*

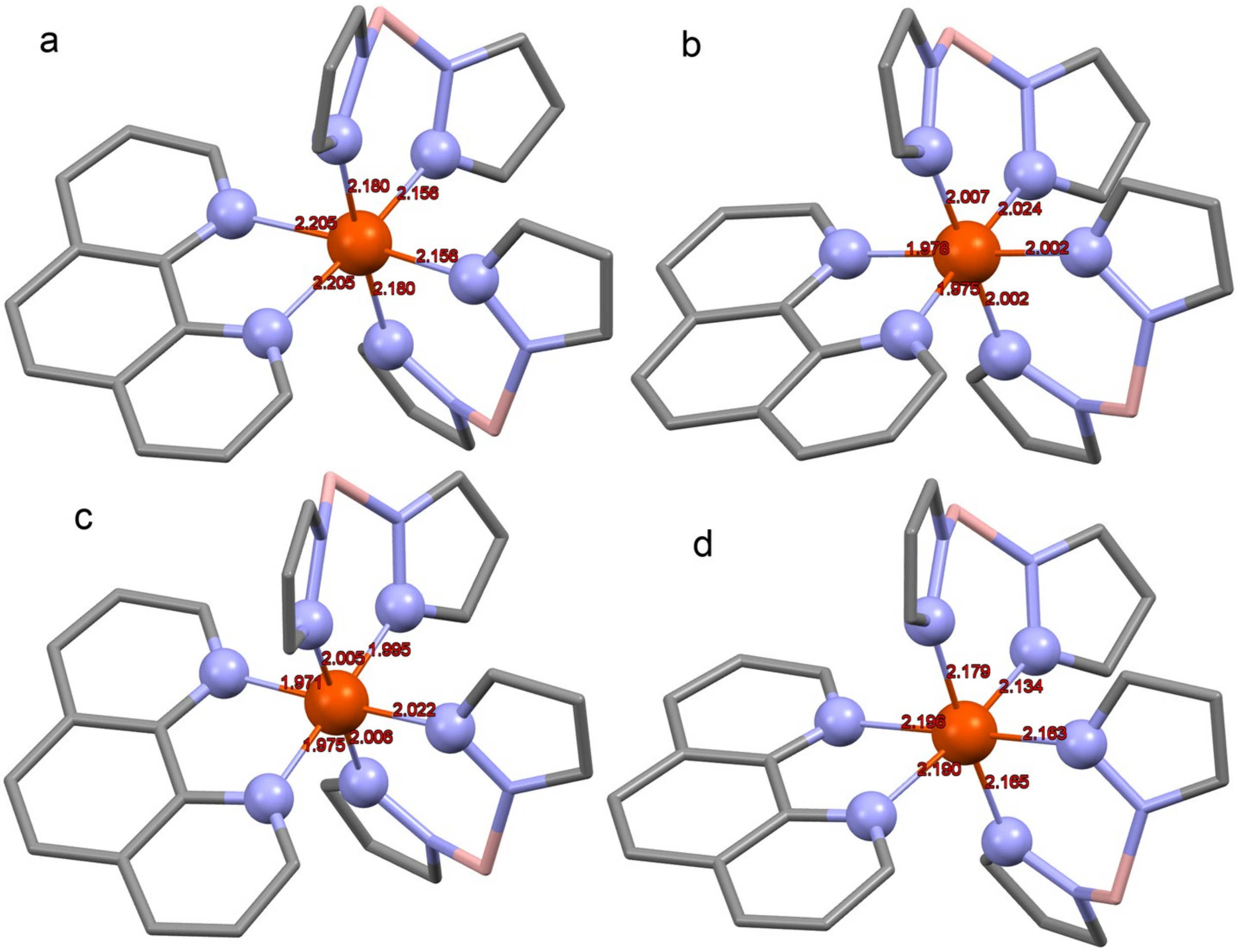

***Figure S16.*** *X-ray diffraction structures of* ***1*** *and Fe-N bond lengths a) at 200 K in the HS state (NEFSUM01 CSD code, oC2/c spacegroup); b) at 100 K in the LS state (NEFSUM02, aP-*1*); c) at 30 K in the LS state (NEFSUM03, aP-*1*); d) at 30 K in the HS state (NEFSUM04, aP-*1*, after photoirradiation with red light).*

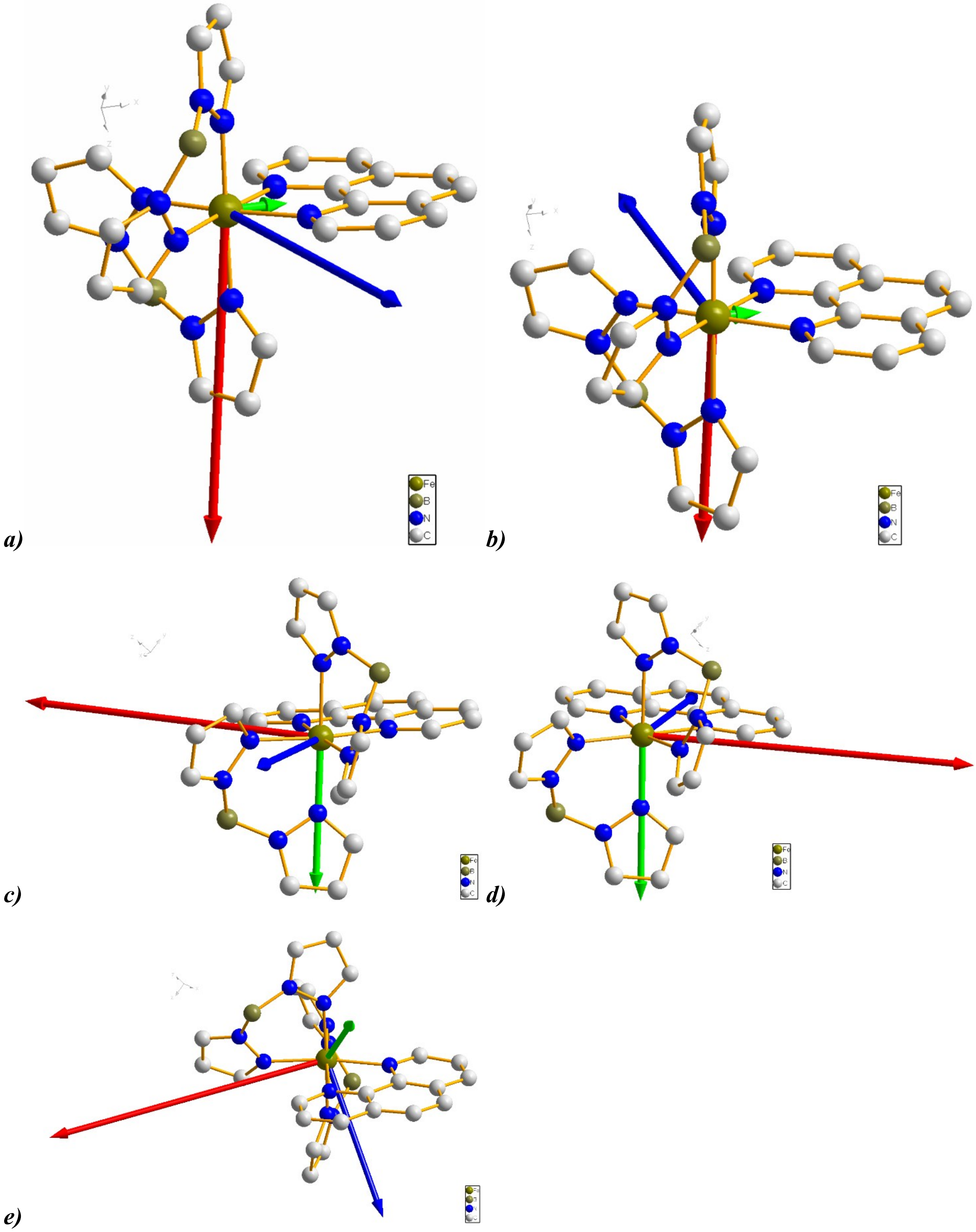

***Figure S17.*** *Representation of the Electric Field Gradient eigenvectors respective to the molecular framework for a) the singlet crystal structure at 100 K, b) the singlet optimized structure, c) the quintet crystal structure at 200 K, d) the quintet optimized structure, e) the quintet crystal structure at 30 K. For singlet structures* $V_{ZZ}$ *corresponds to the blue vector, while for quintet structures it corresponds to the red vector.*

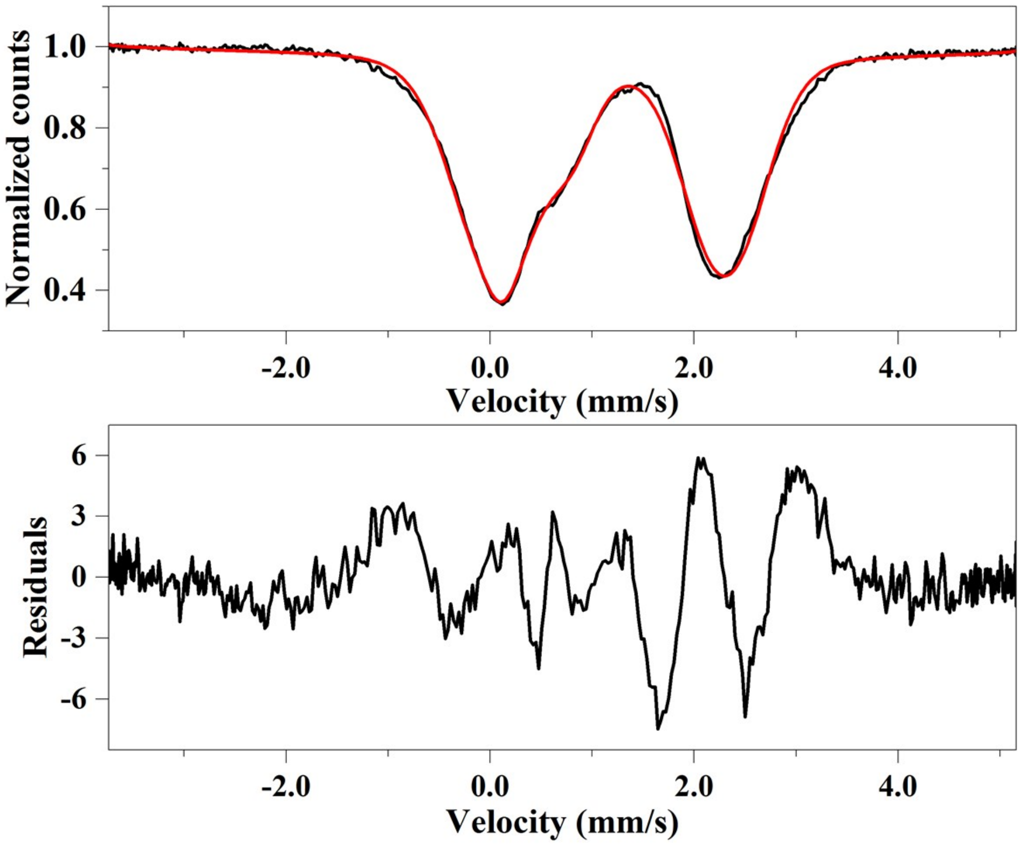

***Figure S18.*** *Top panel: SMS spectrum of the 50 nm thick sublimated sample at 6.0 K after 2.5 hours of irradiation (measured spectrum in black and relative fit in red). Bottom panel: residuals of the fitting procedure.*

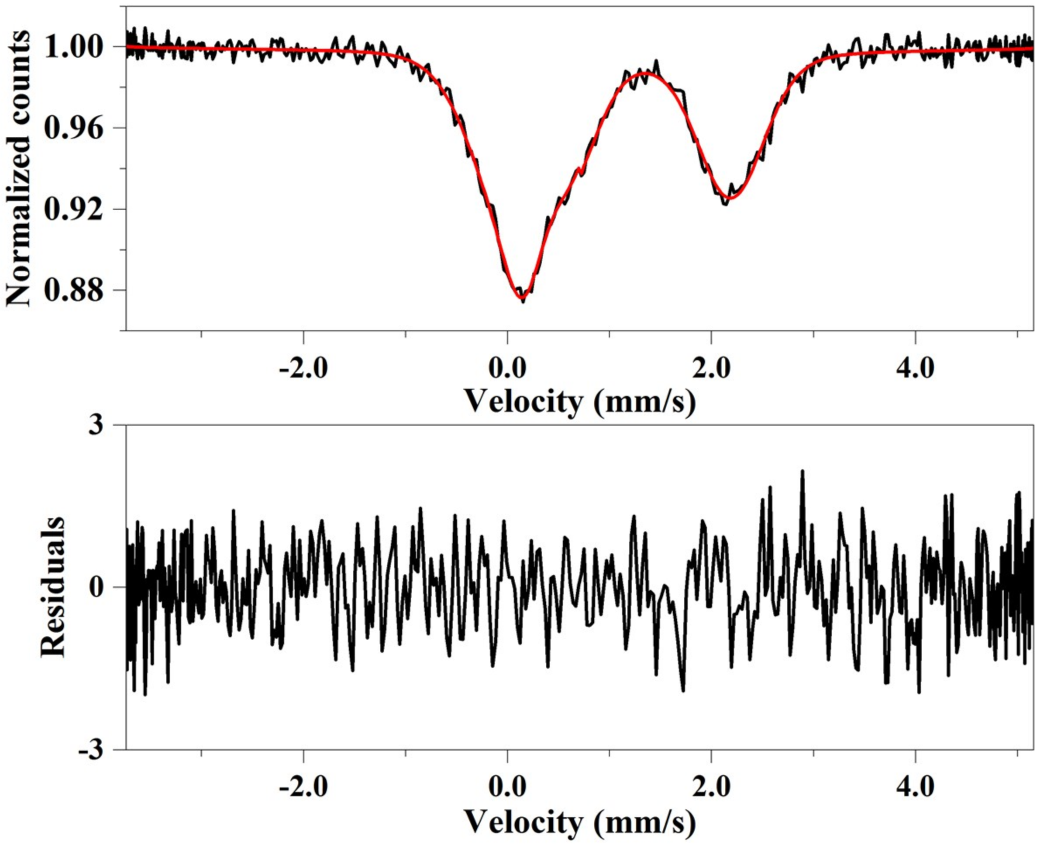

***Figure S19.*** *Top panel: SMS spectrum of the 5 nm thick sublimated sample at 3.0 K after 3.0 hours of irradiation (measured spectrum in black and relative fit in red). Bottom panel: residuals of the fitting procedure.*

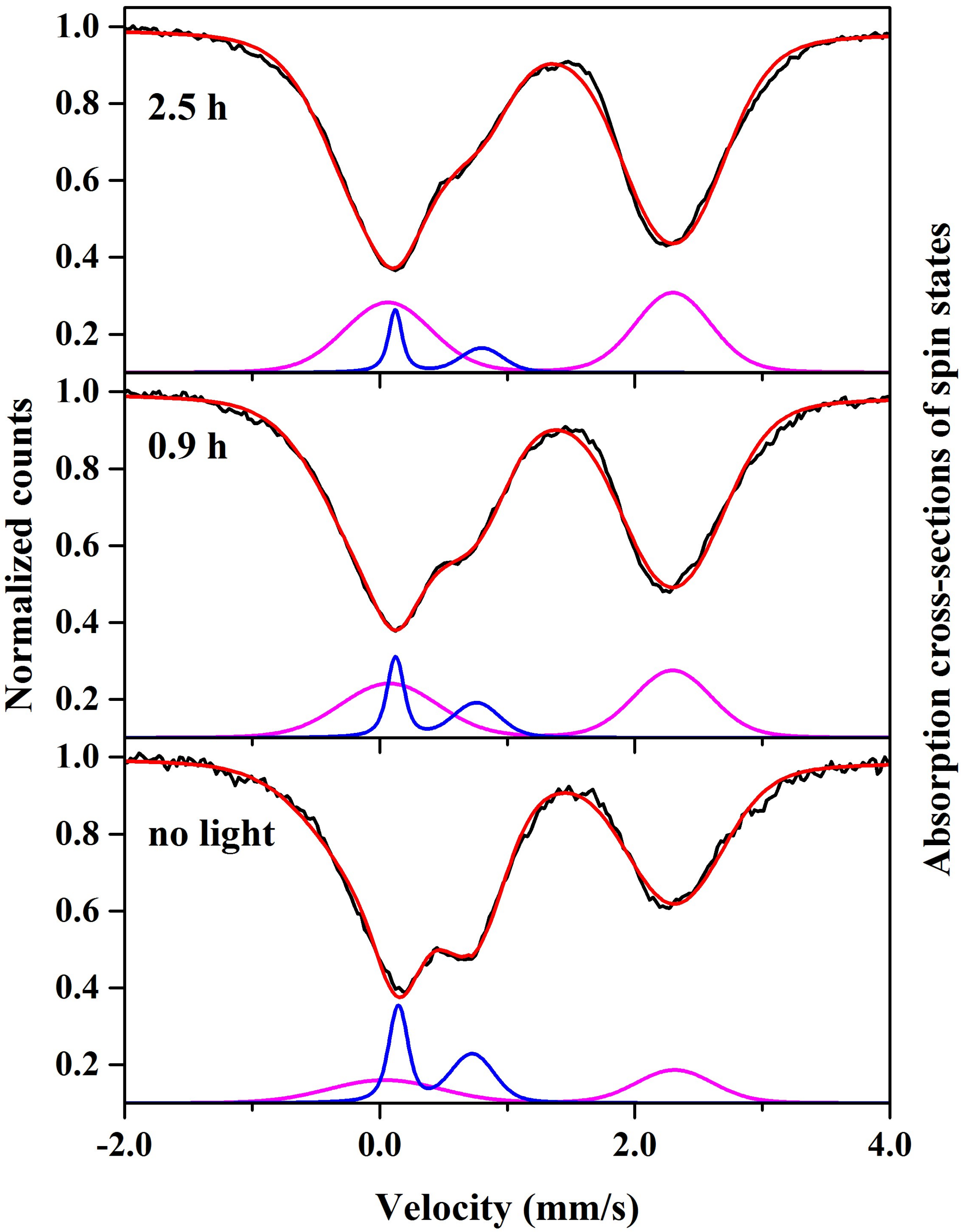

***Figure S20.*** *Experimental spectra (black lines) and best fit curves (red lines) of the 50 nm thick sublimated sample at 6.0 K before the irradiation (0 h) and after two different irradiation times. The absorption cross-sections associated to the HS state (magenta line) and the LS state (blue line) are also shown. The velocity range is restricted to values showing a transmission different from unity.*

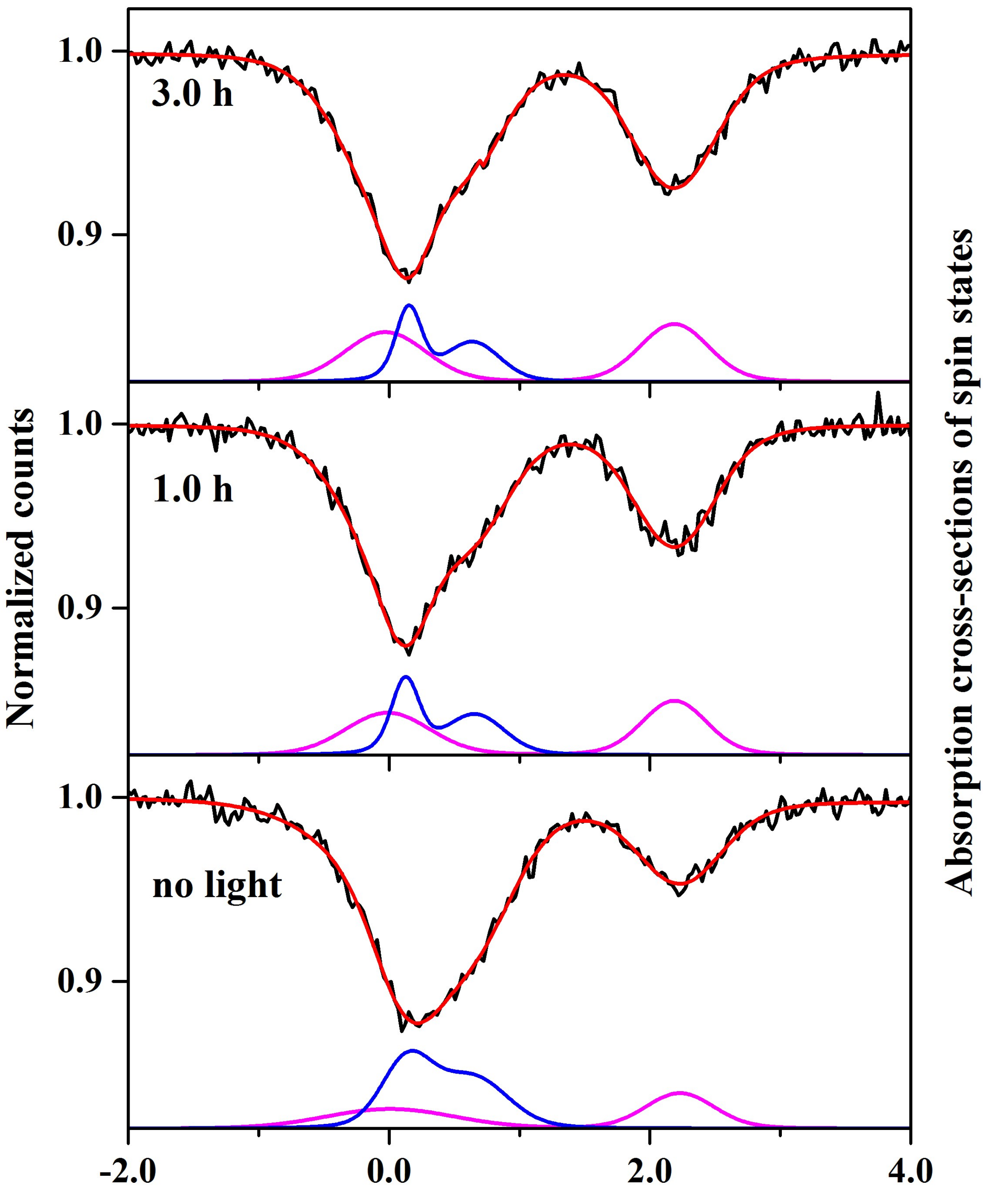

***Figure S21.*** *Experimental spectra (black lines) and best fit curves (red lines) of the 5 nm thick sublimated sample at 3.0 K before the irradiation (0 h) and after two different irradiation times. The absorption cross-sections associated to the HS state (magenta line) and the LS state (blue line) are also shown. The velocity range is restricted to values showing a transmission different from unity.*

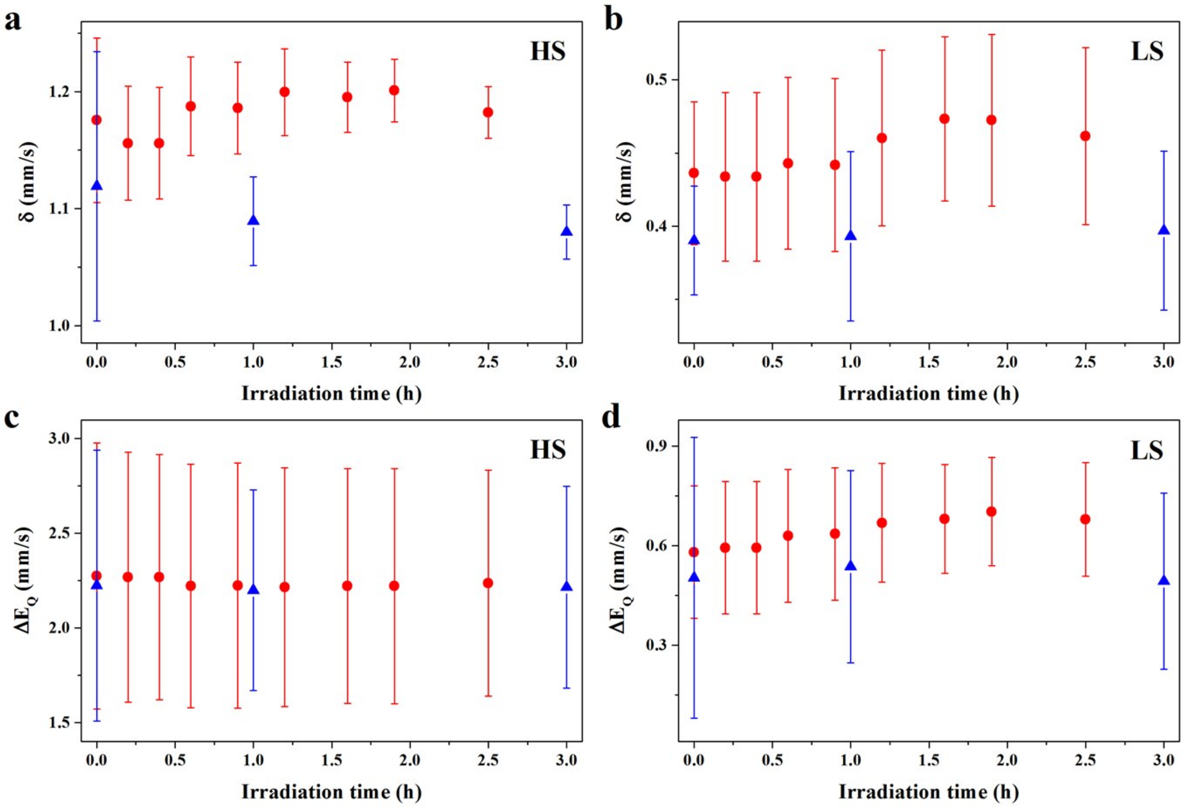

***Figure S22.*** *Hyperfine parameters as a function of the irradiation time with 986 nm wavelength extracted from the fit of the Mössbauer spectra of the 50 nm thick sample (red dots) and the 5 nm thick sample (blue triangles). Isomer shift with respect to α-Fe (a) and quadrupole splitting (c) of the HS state. Isomer shift with respect to α-Fe (b) and quadrupole splitting (d) of the LS state. The distributions are reported as bar around the mean value.*

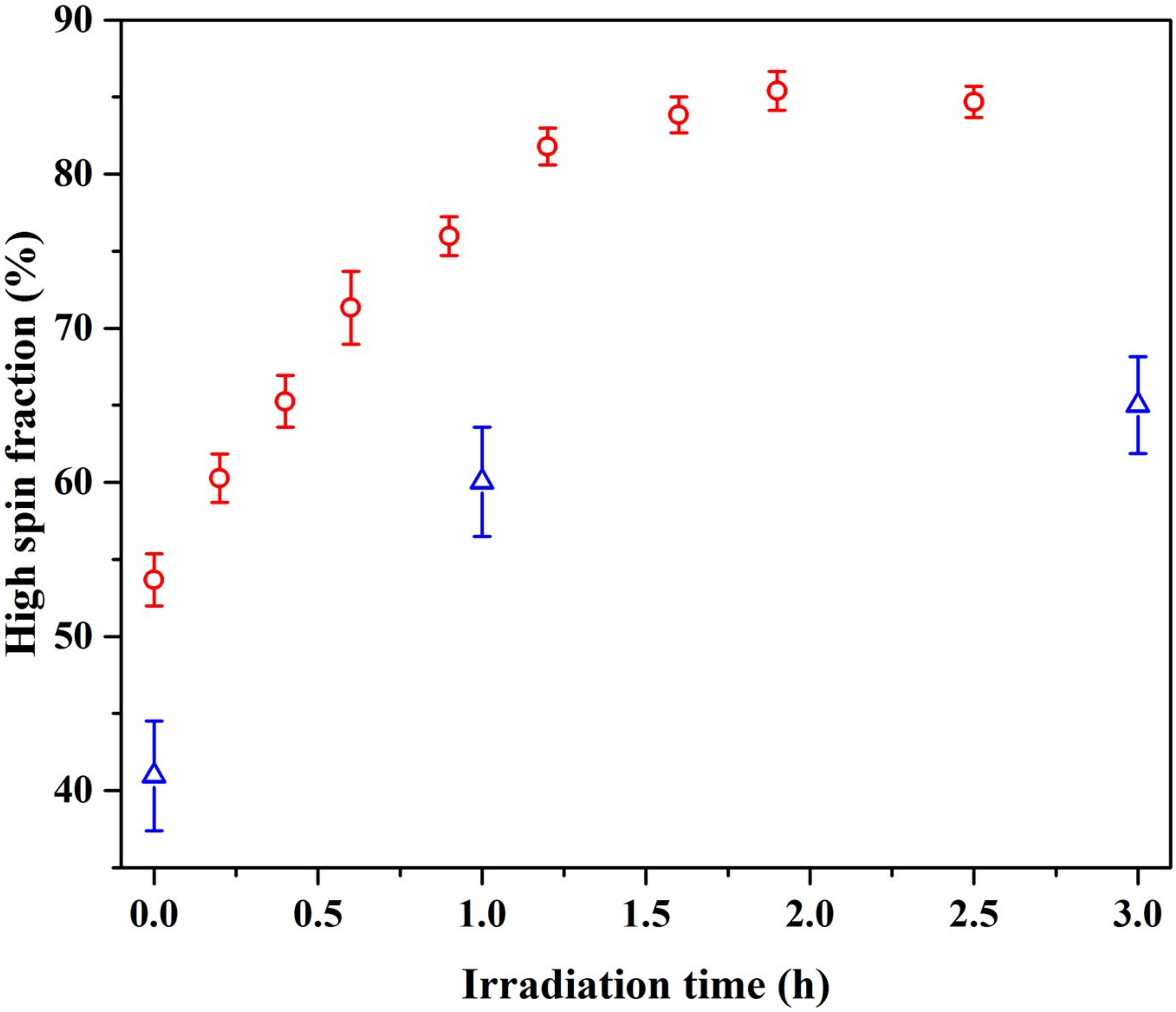

***Figure S23.*** *HS fraction of the 50 nm (red dots) and 5 nm (blue triangles) thick sublimated samples as a function of the irradiation time.*

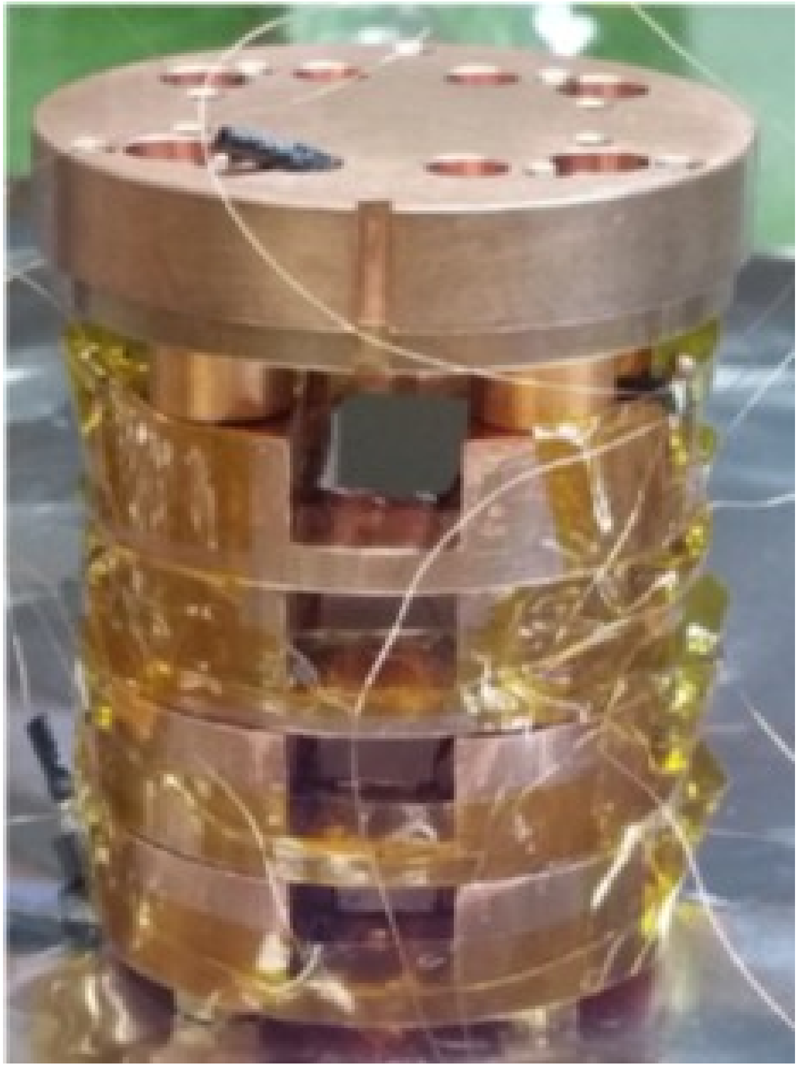

***Figure S24.*** *Modified sample holders with LEDs and connections.*

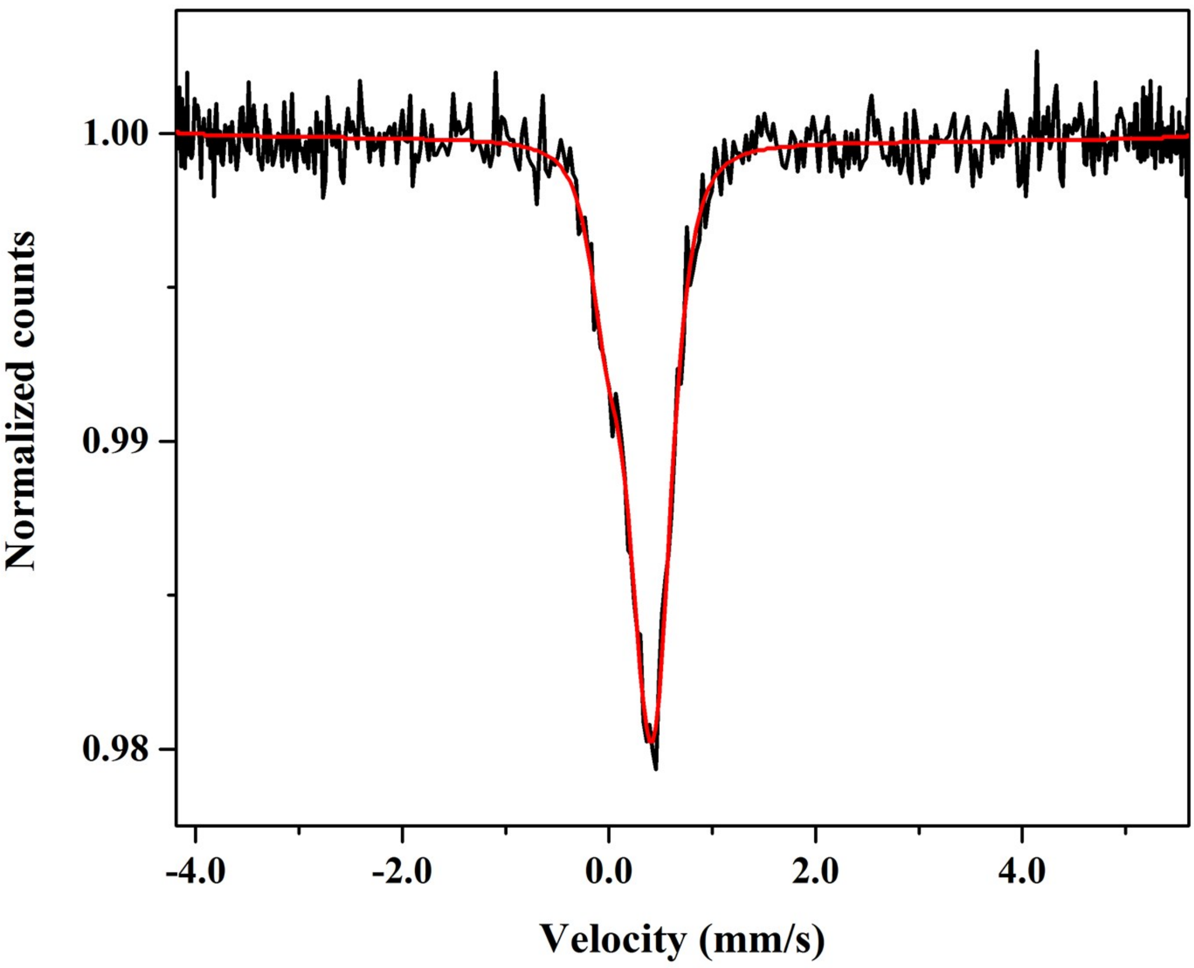

***Figure S25.*** *"Empty-can" Mössbauer spectrum of the beamline (black line) and relative fit (red line).*

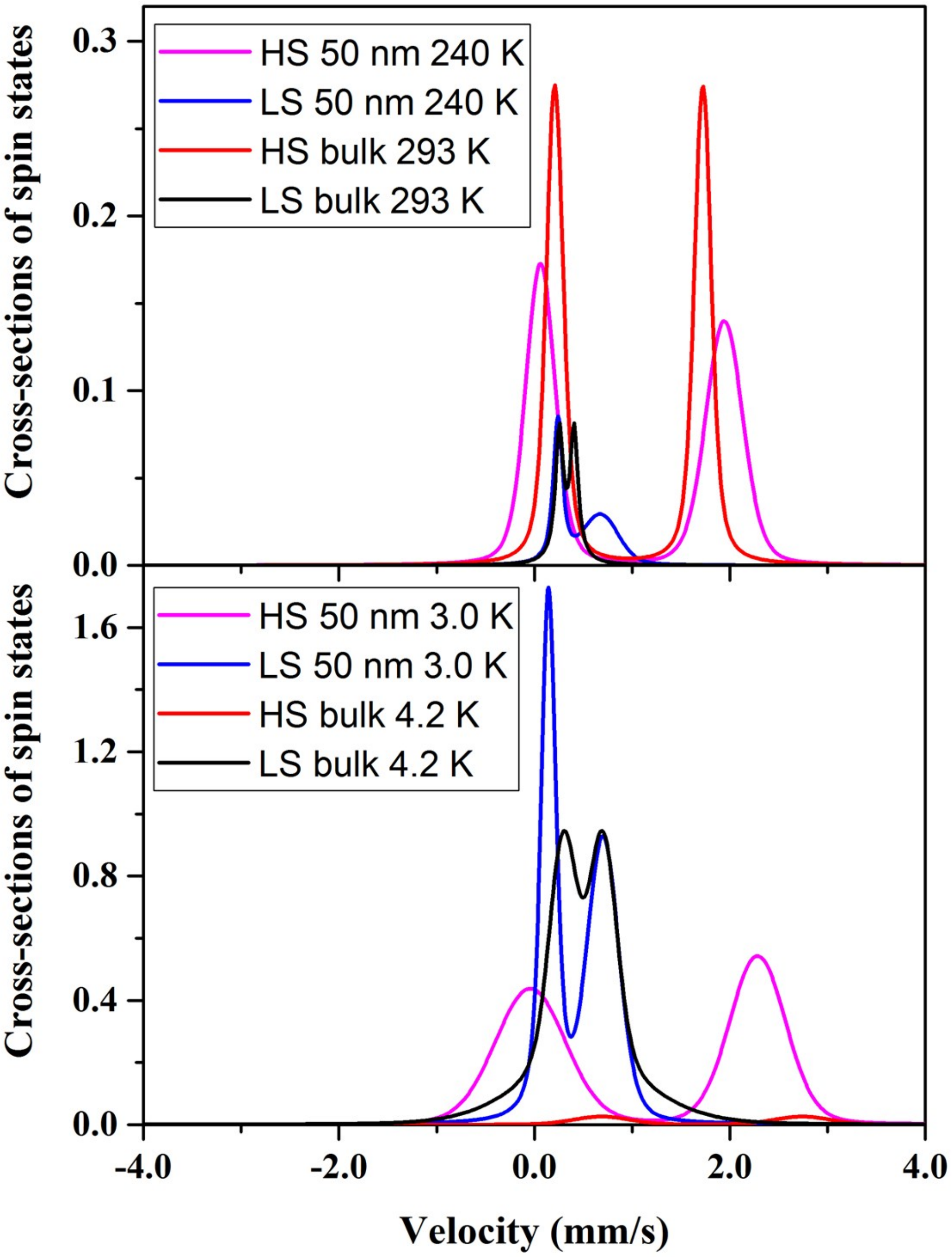

***Figure S26.*** *Comparison between the absorption cross-sections associated to the HS and LS sites extracted from the fit of the spectra of the 50 nm thick sublimated sample and the powder sample at the lowest and highest temperature.*

## S2. Supplementary tables

***Table S1.*** *$^{57}$Fe Mössbauer parameters of the HS and LS states extracted from the fit of the spectra of the powder sample: isomer shift (*$\boldsymbol{\delta_0}$*) and quadrupole splitting (*$\boldsymbol{\Delta E_{Q,0}}$*) mean values, standard deviation (*$\boldsymbol{\sigma}$*) of the Gaussian broadening describing the distribution of values of* $\boldsymbol{\Delta E_Q}$ *and correlation coefficient (*$\boldsymbol{\alpha}$*) between* $\boldsymbol{\delta}$ *and* $\boldsymbol{\Delta E_Q}$*. The calculated HS fraction (%HS) is also shown.*

At each temperature, a majority species, that is attributed to a spin state of the sample (HS state at 293 K and LS state at 4.2 K), and a minor impurity are present. The presence of similar impurities has already been observed in powder samples of the Fe(phen) SCO complex.[1]

| | HS STATE | | | | IMPURITY | | | | |
|---|---|---|---|---|---|---|---|---|---|
| ***T*** (K) | $\boldsymbol{\delta_0}$ (mm/s) | $\boldsymbol{\Delta E_{Q,0}}$ (mm/s) | $\boldsymbol{\sigma}$ (mm/s) | $\boldsymbol{\alpha}$ | $\boldsymbol{\delta_0}$ (mm/s) | $\boldsymbol{\Delta E_{Q,0}}$ (mm/s) | $\boldsymbol{\sigma}$ (mm/s) | $\boldsymbol{\alpha}$ | % |
| 293 | 0.9671(5) | 1.514(1) | 0.0641(7) | 0 | 0.332(3) | 0.151(4) | 0.00002 | 0 | 13(1) |

| | LS STATE | | | | IMPURITY | | | | |
|---|---|---|---|---|---|---|---|---|---|
| ***T*** (K) | $\boldsymbol{\delta_0}$ (mm/s) | $\boldsymbol{\Delta E_{Q,0}}$ (mm/s) | $\boldsymbol{\sigma}$ (mm/s) | $\boldsymbol{\alpha}$ | $\boldsymbol{\delta_0}$ (mm/s) | $\boldsymbol{\Delta E_{Q,0}}$ (mm/s) | $\boldsymbol{\sigma}$ (mm/s) | $\boldsymbol{\alpha}$ | % |
| 4.2 | 0.5001(9) | 0.4082(9) | 0.1211(8)<br>0.591(8)[a] | 0 | 1.72(2) | 2.05(4) | 0.27(1) | 0 | 4.3(2) |

[a] Two LS sites were considered having same $\boldsymbol{\delta_0}$ and $\boldsymbol{\Delta E_{Q,0}}$ and different $\boldsymbol{\sigma}$.

Parameters with no error were kept fixed in the fitting procedure.

***Table S2.*** *Gaussian broadenings of the linewidths associated with each spin doublet calculated from the Gaussian broadening of the quadrupole splitting and the correlation coefficient extracted from the fit of the spectra of the powder sample.*

| | LS STATE | | HS STATE | |
|---|---|---|---|---|
| ***T*** (K) | $\boldsymbol{\sigma_1}$ (mm/s) | $\boldsymbol{\sigma_2}$ (mm/s) | $\boldsymbol{\sigma_1}$ (mm/s) | $\boldsymbol{\sigma_2}$ (mm/s) |
| 293 | | | 0.0641(7) | 0.0641(7) |
| 4.2 | 0.1211(8)<br>0.591(8)[a] | 0.1211(8)<br>0.591(8)[a] | | |

[a] Two LS sites were considered having same $\boldsymbol{\delta_0}$ and $\boldsymbol{\Delta E_{Q,0}}$ and different $\boldsymbol{\sigma}$.

***Table S3.*** *$^{57}$Fe Mössbauer parameters of the HS and LS states extracted from the fit of the spectra of the dropcast sample: isomer shift (*$\boldsymbol{\delta_0}$*) and quadrupole splitting (*$\boldsymbol{\Delta E_{Q,0}}$*) mean values, standard deviation (*$\boldsymbol{\sigma}$*) of the Gaussian broadening describing the distribution of values of* $\boldsymbol{\Delta E_Q}$ *and correlation coefficient (*$\boldsymbol{\alpha}$*) between* $\boldsymbol{\delta}$ *and* $\boldsymbol{\Delta E_Q}$*. The calculated HS fraction (%HS) is also reported.*

| | LS STATE | | | | HS STATE | | | | |
|---|---|---|---|---|---|---|---|---|---|
| ***T*** (K) | $\boldsymbol{\delta_0}$ (mm/s) | $\boldsymbol{\Delta E_{Q,0}}$ (mm/s) | $\boldsymbol{\sigma}$ (mm/s) | $\boldsymbol{\alpha}$ | $\boldsymbol{\delta_0}$ (mm/s) | $\boldsymbol{\Delta E_{Q,0}}$ (mm/s) | $\boldsymbol{\sigma}$ (mm/s) | $\boldsymbol{\alpha}$ | %HS |
| 278 | 0.47(8) | 0.5(2) | 0.088 | 0.79 | 0.975(8) | 1.75(2) | 0.14(1) | 0.08(7) | 91(4) |
| 3.0 | 0.41 | 0.6 | 0.095 | 0.45 | 1.101(1) | 2.311(2) | 0.291(2) | -0.065(5) | 60(1) |

Parameters with no error were kept fixed in the fitting procedure.

***Table S4.*** *Gaussian broadenings of the linewidths associated with each spin doublet calculated from the Gaussian broadening of the quadrupole splitting and the correlation coefficient extracted from the fit of the spectra of the dropcast sample.*

| ***T*** (K) | LS STATE | | HS STATE | |
|---|---|---|---|---|
| | $\sigma_1$ (mm/s) | $\sigma_2$ (mm/s) | $\sigma_1$ (mm/s) | $\sigma_2$ (mm/s) |
| 278 | 0.018 | 0.16 | 0.13(2) | 0.16(2) |
| 3.0 | 0.052 | 0.14 | 0.310(3) | 0.272(3) |

***Table S5.*** *$^{57}$Fe Mössbauer parameters of the HS and LS states extracted from the fit of the spectra of the 50 nm thick sublimated sample: isomer shift ($\delta_0$) and quadrupole splitting ($\Delta E_{Q,0}$) mean values, standard deviation ($\sigma$) of the Gaussian broadening describing the distribution of values of $\Delta E_Q$ and correlation coefficient ($\alpha$) between $\delta$ and $\Delta E_Q$. The calculated HS fraction (%HS) is also reported.*

| ***T*** (K) | LS STATE | | | | HS STATE | | | | %HS |
|---|---|---|---|---|---|---|---|---|---|
| | $\delta_0$ (mm/s) | $\Delta E_{Q,0}$ (mm/s) | $\sigma$ (mm/s) | $\alpha$ | $\delta_0$ (mm/s) | $\Delta E_{Q,0}$ (mm/s) | $\sigma$ (mm/s) | $\alpha$ | |
| 240 | 0.46(2) | 0.44(3) | 0.088 | 0.79 | 1.003(4) | 1.880(8) | 0.148(6) | 0.14 | 84(3) |
| 198 | 0.44(3) | 0.49(6) | 0.088 | 0.79 | 1.05(1) | 2.01(2) | 0.20(2) | 0.14(7) | 78(6) |
| 156 | 0.424(8) | 0.58(2) | 0.088 | 0.79 | 1.094(6) | 2.11(1) | 0.239(6) | -0.08(2) | 71(3) |
| 105 | 0.425(3) | 0.578(4) | 0.088 | 0.79 | 1.127(4) | 2.292(8) | 0.307(4) | -0.16(1) | 56(1) |
| 65 | 0.426(3) | 0.564(4) | 0.088 | 0.79 | 1.144(7) | 2.36(1) | 0.329(5) | -0.19(1) | 48(1) |
| 17 | 0.429 | 0.588 | 0.088 | 0.79 | 1.163(2) | 2.293(3) | 0.344(2) | -0.171(4) | 57(1) |
| 3.0 | 0.425(2) | 0.558(3) | 0.096(3) | 0.45(6) | 1.122(2) | 2.324(5) | 0.303(3) | -0.122(9) | 50(1) |

Parameters with no error were kept fixed in the fitting procedure.

***Table S6.*** *Gaussian broadenings of the linewidths associated with each spin doublet calculated from the Gaussian broadening of the quadrupole splitting and the correlation coefficient extracted from the fit of the spectra of the 50 nm thick sublimated sample.*

| ***T*** (K) | LS STATE | | HS STATE | |
|---|---|---|---|---|
| | $\sigma_1$ (mm/s) | $\sigma_2$ (mm/s) | $\sigma_1$ (mm/s) | $\sigma_2$ (mm/s) |
| 240 | 0.018 | 0.16 | 0.13(4) | 0.168(7) |
| 198 | 0.018 | 0.16 | 0.17(3) | 0.23(3) |
| 156 | 0.018 | 0.16 | 0.26(1) | 0.219(9) |
| 105 | 0.018 | 0.16 | 0.355(8) | 0.259(7) |
| 65 | 0.018 | 0.16 | 0.39(1) | 0.266(8) |
| 17 | 0.018 | 0.16 | 0.403(4) | 0.285(3) |
| 3.0 | 0.053(7) | 0.14(4) | 0.340(6) | 0.266(6) |

***Table S7.*** *$^{57}$Fe Mössbauer parameters of the HS and LS states extracted from the fit of the spectra of the 5 nm thick sublimated sample: isomer shift (***$\delta_0$***) and quadrupole splitting (***$\Delta E_{Q,0}$***) mean values, standard deviation (***$\sigma$***) of the Gaussian broadening describing the distribution of values of* **$\Delta E_Q$** *and correlation coefficient (***$\alpha$***) between* **$\delta$** *and* **$\Delta E_Q$***. The calculated HS fraction (%HS) is also reported.*

| ***T*** (K) | LS STATE | | | | HS STATE | | | | %HS |
|---|---|---|---|---|---|---|---|---|---|
| | **$\delta_0$** (mm/s) | **$\Delta E_{Q,0}$** (mm/s) | **$\sigma$** (mm/s) | **$\alpha$** | **$\delta_0$** (mm/s) | **$\Delta E_{Q,0}$** (mm/s) | **$\sigma$** (mm/s) | **$\alpha$** | |
| 177 | 0.26(7) | 0.2(2) | 0.23(7) | 0.4(1) | 1.11(7) | 1.9(1) | 0.35(4) | -0.16 | 58(8) |
| 99 | 0.35(2) | 0.50(2) | 0.17(1) | 0.32(4) | 1.11(3) | 2.13(5) | 0.38(4) | -0.36(7) | 48(3) |
| 8.0 | 0.420(9) | 0.518(8) | 0.126(8) | 0.27(5) | 1.10(1) | 2.25(3) | 0.30(2) | -0.23(5) | 43(2) |
| 3.0 | 0.39(2) | 0.50(1) | 0.21(2) | 0.18(3) | 1.12(4) | 2.22(7) | 0.36(4) | -0.32(9) | 41(4) |

Parameters with no error were kept fixed in the fitting procedure.

***Table S8.*** *Gaussian broadenings of the linewidths associated with each spin doublet calculated from the Gaussian broadening of the quadrupole splitting and the correlation coefficient extracted from the fit of the spectra of the 5 nm thick sublimated sample.*

| ***T*** (K) | LS STATE | | HS STATE | |
|---|---|---|---|---|
| | **$\sigma_1$** (mm/s) | **$\sigma_2$** (mm/s) | **$\sigma_1$** (mm/s) | **$\sigma_2$** (mm/s) |
| 177 | 0.13(7) | 0.3(1) | 0.41(4) | 0.29(3) |
| 99 | 0.11(2) | 0.22(2) | 0.51(7) | 0.24(5) |
| 8.0 | 0.09(1) | 0.16(2) | 0.36(4) | 0.23(3) |
| 3.0 | 0.17(2) | 0.25(2) | 0.47(9) | 0.24(6) |

***Table S9.*** *$^{57}$Fe Mössbauer parameters of the HS and LS states extracted from the fit of the spectra of the 50 nm thick sublimated sample in function of the irradiation time: isomer shift (***$\delta_0$***) and quadrupole splitting (***$\Delta E_{Q,0}$***) mean values, standard deviation (***$\sigma$***) of the Gaussian broadening describing the distribution of values of* **$\Delta E_Q$** *and correlation coefficient (***$\alpha$***) between* **$\delta$** *and* **$\Delta E_Q$***. The calculated HS fraction (%HS) is also reported.*

| Time (h) | LS STATE | | | | HS STATE | | | | %HS |
|---|---|---|---|---|---|---|---|---|---|
| | **$\delta_0$** (mm/s) | **$\Delta E_{Q,0}$** (mm/s) | **$\sigma$** (mm/s) | **$\alpha$** | **$\delta_0$** (mm/s) | **$\Delta E_{Q,0}$** (mm/s) | **$\sigma$** (mm/s) | **$\alpha$** | |
| 0 | 0.436(6) | 0.581(7) | 0.100(7) | 0.5(1) | 1.176(7) | 2.27(1) | 0.351(9) | -0.20(2) | 54(2) |
| 0.2 | 0.434(4) | 0.594(5) | 0.100(7) | 0.6(1) | 1.156(5) | 2.268(9) | 0.330(5) | -0.15(1) | 60(2) |
| 0.4 | 0.434(6) | 0.59(1) | 0.100(8) | 0.6(2) | 1.156(5) | 2.27(1) | 0.324(5) | -0.15(1) | 65(2) |
| 0.6 | 0.443(6) | 0.63(1) | 0.10(1) | 0.6(3) | 1.187(6) | 2.22(1) | 0.322(5) | -0.13(2) | 71(2) |
| 0.9 | 0.442(4) | 0.635(6) | 0.100(6) | 0.6(1) | 1.186(3) | 2.223(5) | 0.324(2) | -0.121(6) | 76(1) |
| 1.2 | 0.460(4) | 0.669(8) | 0.09(2) | 0.7(3) | 1.200(2) | 2.215(5) | 0.315(2) | -0.117(7) | 82(1) |
| 1.6 | 0.473(4) | 0.681(9) | 0.08(2) | 0.7(4) | 1.195(2) | 2.221(4) | 0.310(2) | -0.097(7) | 84(1) |
| 1.9 | 0.472(4) | 0.70(1) | 0.08(3) | 0.7(6) | 1.201(2) | 2.221(4) | 0.311(2) | -0.086(7) | 85(1) |
| 2.5 | 0.462(4) | 0.680(9) | 0.09(2) | 0.7(4) | 1.182(2) | 2.236(3) | 0.298(2) | -0.074(5) | 85(1) |

***Table S10.*** *Gaussian broadenings of the linewidths associated with each spin doublet calculated from the Gaussian broadening of the quadrupole splitting and the correlation coefficient extracted from the fit of the spectra of the 50 nm thick sample.*

| Time (h) | LS STATE | | HS STATE | |
|---|---|---|---|---|
| | **$\sigma_1$** (mm/s) | **$\sigma_2$** (mm/s) | **$\sigma_1$** (mm/s) | **$\sigma_2$** (mm/s) |
| 0 | 0.05(2) | 0.15(3) | 0.42(2) | 0.28(1) |
| 0.2 | 0.04(2) | 0.16(2) | 0.38(1) | 0.281(9) |
| 0.4 | 0.04(2) | 0.16(3) | 0.37(1) | 0.276(8) |
| 0.6 | 0.04(3) | 0.16(5) | 0.36(1) | 0.279(9) |
| 0.9 | 0.04(1) | 0.16(2) | 0.363(5) | 0.285(4) |
| 1.2 | 0.03(3) | 0.15(6) | 0.352(5) | 0.278(4) |
| 1.6 | 0.03(4) | 0.14(7) | 0.341(5) | 0.280(4) |
| 1.9 | 0.02(6) | 0.14(9) | 0.337(5) | 0.284(4) |
| 2.5 | 0.03(4) | 0.15(6) | 0.320(3) | 0.276(3) |

***Table S11.*** *$^{57}$Fe Mössbauer parameters of the HS and LS states extracted from the fit of the spectra of the 5 nm thick sublimated sample in function of the irradiation time: isomer shift (**$\delta_0$**) and quadrupole splitting (**$\Delta E_{Q,0}$**) mean values, standard deviation (**$\sigma$**) of the Gaussian broadening describing the distribution of values of **$\Delta E_Q$** and correlation coefficient (**$\alpha$**) between **$\delta$** and **$\Delta E_Q$**. The calculated HS fraction (%HS) is also reported.*

| Time (h) | LS STATE | | | | HS STATE | | | | %HS |
|---|---|---|---|---|---|---|---|---|---|
| | **$\delta_0$** (mm/s) | **$\Delta E_{Q,0}$** (mm/s) | **$\sigma$** (mm/s) | **$\alpha$** | **$\delta_0$** (mm/s) | **$\Delta E_{Q,0}$** (mm/s) | **$\sigma$** (mm/s) | **$\alpha$** | |
| 0 | 0.39(2) | 0.50(1) | 0.21(2) | 0.18(3) | 1.12(4) | 2.22(7) | 0.36(4) | -0.32(9) | 41(4) |
| 1.0 | 0.39(2) | 0.54(2) | 0.14(2) | 0.4(1) | 1.09(1) | 2.20(3) | 0.27(2) | -0.14(6) | 60(4) |
| 3.0 | 0.40(2) | 0.49(2) | 0.13(2) | 0.41(9) | 1.080(9) | 2.21(2) | 0.27(1) | -0.09(4) | 65(3) |

***Table S12.*** *Gaussian broadenings of the linewidths associated with each spin doublet calculated from the Gaussian broadening of the quadrupole splitting and the correlation coefficient extracted from the fit of the spectra of the 5 nm thick sample.*

| Time (h) | LS STATE | | HS STATE | |
|---|---|---|---|---|
| | **$\sigma_1$** (mm/s) | **$\sigma_2$** (mm/s) | **$\sigma_1$** (mm/s) | **$\sigma_2$** (mm/s) |
| 0 | 0.17(2) | 0.25(2) | 0.47(9) | 0.24(6) |
| 1.0 | 0.09(3) | 0.20(4) | 0.30(4) | 0.23(3) |
| 3.0 | 0.08(2) | 0.19(3) | 0.29(2) | 0.24(2) |

## S3. Note S1

A relevant issue is the strong asymmetry in the absorption cross-section of the LS state (see Figures 4 and S14), due to a high correlation between the isomer shift and quadrupole splitting distributions. Similar considerations hold also for the HS state, although the asymmetry is less pronounced. Correlations are similar for both sublimated samples, irrespective of their thickness. The possible presence of theses correlations in the bulk phase was checked by treating through the same procedure (i.e. same hypotheses on the absorption cross-section of the sample) the data measured on a standard setup on the initial powder sample of $^{57}$**1**. The fit of the Mössbauer spectra at both 293 K and 4.2 K (see Figure S2 and corresponding values in Table S1) showed that there are no correlations between the quadrupole splitting and the isomer shift (*i.e.* $\boldsymbol{\alpha} = 0$). The absorption cross-sections of the HS and LS sites result to be symmetric and narrower than those extracted from the fit of the sublimated samples, as well as of the dropcast (see Figure S26). Therefore, the correlation found in the spectra of the sublimated samples is likely to be induced by the interaction with the surface and would indicate a heterogeneity of the crystal field that allows a partial delocalization of electron density on the $e_g$ levels, which ultimately modifies the switching properties. These distances are very much dependent on the substrate/molecule nature and interaction, as shown by the differences seen on the closely related compound with 2,2'-bipyridine substituting the phen ligand, on either gold[2] or highly-ordered pyrolytic graphite.[3]

## S4. Note S2

As said in the main text, the observed distributions in the Fe-ligands distances are about one order of magnitude lower than the general accepted changes in the Fe-ligands distances associated with the transition between HS and LS states in bulk phase, represented in Figure S16. But one must keep in mind though that diffraction yields a picture that is an average both in time, due to the timescale of a typical diffraction data collection, and in space. While the heteroleptic nature of the complex prevents a description in a pure octahedral framework, when considering each bidentate ligand (bpz and phen) it can be readily seen that indeed in the LS state both ligands are rather symmetrically coordinated to the iron ion (the difference between the two Fe-N bonds of each ligand Δ(Fe-N) are ≤ 0.017 Å both at 100 K and 30 K). In the HS structure at 200 K the coordination of the phen ligand to the Fe ion is perfectly symmetrical due to the twofold-symmetry axis imposed by the crystalline symmetry of 1 (*C*2/*c* spacegroup) going through the ligand and the Fe ion, while for both the bpz ligands the dissymmetry is quite pronounced (Δ(Fe-N) = 0.024 Å). Similar results are found for the HS photoinduced state at 30 K: Δ(Fe-N) = 0.006 Å for phen, while Δ(Fe-N) = 0.002 Å and 0.045 Å for the bpz ligands.

## S5. Note S3

DFT calculations using the Gaussian16 quantum chemical program[4] were carried out using the B3LYP functional, the relativistic electron-core double-ζ LANL2DZ pseudopotentials for iron and the 6-311++G(d,p) Gaussian basis set for remaining atoms. Either single-point calculations on coordinates extracted from the known X-ray crystal structures[5] or full optimizations were performed. Calculated traceless Electric Field Gradient (EFG) tensors were diagonalized and eigenvalues ranked as $|V_{ZZ}|>|V_{YY}|>|V_{XX}|$, and quadrupole splittings derived using the reported formula:[6]

$$\Delta\left(\frac{mm}{s}\right) = \frac{1}{2}eQV_{ZZ}\sqrt{1+\frac{\eta^2}{3}\frac{c}{E}} = -1.618_{\pm 0.101} \times V_{ZZ}\sqrt{1+\frac{\eta^2}{3}}$$

$$\eta = \frac{V_{XX} - V_{YY}}{V_{ZZ}}$$

with eigenvalues in SI units (1 au = $9.717\times10^{21}$ V/m$^2$) and considering for the $^{57}$Fe quadrupolar moment value $Q$ 0.16(1) m$^2$.[6] The high relative uncertainty on the value of $Q$ translates directly to uncertainties between 0.1 and 0.2 mm/s on calculated Δ.

Geometry optimization was performed after removing the twofold symmetry for both the singlet and quintet state, and final geometries stayed very close to the initial twofold symmetry. In the quintet case, actually starting from a much less symmetrical structure prevented convergence.

Geometries details and corresponding EFG tensors and quadrupole splittings are given in the two following tables, and the EFG tensor eigenvectors represented respective to the molecular frameworks in Figure S17.

We checked our calculations with the optimization of the $[Fe(HBpz_3)_2]$ complex (in C1 symmetry) and verified that the geometry we found is undistinguishable from the one reported in the literature. We found -3.57(22) mm/s for Δ, with η very close to 0, very similar values to both DFT (-3.568 to -3.717 mm/s) and experimental (-3.44(2) mm/s) values reported previously.[6] The eigenvector corresponding to $V_{ZZ}$ was found to lie along the pseudo-threefold axis (the B···Fe···B direction). We also checked the existence of critical behaviors by optimizing the almost identical complex $[Fe(HCpz_3)_2]^{2+}$ (in Ci symmetry). Results are very similar, with η very close to 0 and -3.61(22) mm/s for Δ, which compares badly to a reported value of 2.20 mm/s.[7]

Both single-point calculations on coordinates extracted from the known X-ray crystal structures[5] and a full optimization were performed (see geometrical details in Table S13). The resulting estimations of the quadrupole splitting are reported in Table S14. For the LS state the calculated values are in the range 0.2 - 0.3 mm/s, therefore below the experimental values, although in line with previous results on a closely related SCO compound.[6] For the HS state the calculated values are very sensitive to the geometry, varying between 2.8 mm/s and 3.6 mm/s, but in all cases quite above the experimental values. The detected disagreement between experimental and calculated data is however not surprising, since an over- or under- estimation of the values of the quadrupole splitting calculated by DFT has already been reported for other SCO complexes.[7,8] Despite this critical evaluation of the eigenvalues, it is quite instructive to visualize the calculated EFG eigenvectors in the molecular framework (see Figure S17). The LS state could be compared to easy plane anisotropy, with the smallest component $V_{XX}$ lying along the approximate twofold symmetry axis of the complex and $V_{ZZ}$ perpendicular to this axis, lying close to the mean plane of the phen ligand. Moreover, $V_{YY}$ is very close in value to $V_{ZZ}$ and lies perpendicular to the phen ligand and very close to the pz-Fe-pz axis. Concerning the HS state, in the twofold-symmetric high-temperature structure or the unsymmetric optimized structure, $V_{ZZ}$ lies close to the phen mean plane perpendicularly to the approximate twofold symmetry axis, quite similarly to that of the LS state. A different picture emerges when considering the photoinduced HS state in the 30 K crystal structure, which is clearly the most deformed one (see in Table S13 distances between the Fe ion and the various azole mean planes): while $V_{ZZ}$ still makes an angle of only 5.04° with the phen mean plane, it lies much closer to the $N_{pz}$-Fe-$N_{phen}$ axis (at 29.1° *vs* 48.6° at 200 K). Furthermore, the two other eigenvectors point completely away from the approximate two-fold symmetry axis and its perpendicular pz-Fe-pz axis.

***Table S13.*** *Comparison of relevant distances in complex **1** in experimental and optimized structures: $FeN_6$ distances and angles, Fe···B distances and the $H_2Bpz_2$ pz-B-pz angle, Fe distances to mean planes of the ligands two pyridine and the four pyrazole rings, angle between the two pyridine mean planes of the phen ligand.*

| Spin state | Structure | Atoms | <Value>, Range | Optimization change | Planes | Values | Optimization change |
|---|---|---|---|---|---|---|---|
| Singlet | X-ray 100 K($C_1$) | Fe-$N_{phen}$ | 1.977, 0.003Å | | Fe···plane(py) | -0.086, 0.083Å | |
| | | Fe-$N_{pz}$ | 2.009, 0.022Å | | Fe···plane(pz) | -0.292, -0.268Å | |
| | | Fe···B | 3.433, 0.003Å | | | 0.171, 0.491Å | |
| | | N-Fe-$N_{phen}$ | 82.39° | | $py\hat{\cdots}py$ (phen) | 4.03(13)° | |
| | | N-Fe-$N_{pz}$ | 92.73, 0.31° | | | | |
| | | N-B-N | 109.60, 1.37° | | | | |
| | Optimized ($C_1$) | Fe-$N_{phen}$ | 2.032, 0.000Å | +0.057Å | Fe···plane(py) | ±0.010 | -0.075Å |
| | | Fe-$N_{pz}$ | 2.049, 0.021Å | +0.040Å | Fe···plane(pz) | ±(0.206, 0.294)Å | |
| | | Fe···B | 3.448, 0.000Å | +0.015Å | $py\hat{\cdots}py$ (phen) | 0.13° | -3.90° |
| | | N-Fe-$N_{phen}$ | 81.44° | -0.95° | | | |
| | | N-Fe-$N_{pz}$ | 90.93, 0.00° | -1.80° | | | |
| | | N-B-N | 109.22, 0.00° | -0.38° | | | |
| Quintet | X-ray 200 K ($C_2$) | Fe-$N_{phen}$ | 2.205, 0.000Å | | Fe···plane(py) | ±0.173 | |
| | | Fe-$N_{pz}$ | 2.168, 0.024Å | | Fe···plane(pz) | ±(0.443, 0.734)Å | |
| | | Fe···B | 3.516, 0.000Å | | $py\hat{\cdots}py$ (phen) | 5.52(11)° | |
| | | N-Fe-$N_{phen}$ | 75.02° | | | | |
| | | N-Fe-$N_{pz}$ | 90.41° | | | | |
| | | N-B-N | 110.39° | | | | |
| | Optimized ($C_1$) | Fe-$N_{phen}$ | 2.270, 0.000Å | +0.065Å | Fe···plane(py) | ±0.004 | -0.169Å |
| | | Fe-$N_{pz}$ | 2.214, 0.078Å | +0.046Å | Fe···plane(pz) | ±(0.354, 0.614)Å | |
| | | Fe···B | 3.546, 0.000Å | +0.03Å | $py\hat{\cdots}py$ (phen) | 0.12° | -5.40° |
| | | N-Fe-$N_{phen}$ | 73.65° | -1.37° | | | |
| | | N-Fe-$N_{pz}$ | 88.20, 0.00° | -2.21° | | | |
| | | N-B-N | 110.00, 0.00° | -0.39° | | | |
| | X-ray 30 K ($C_1$) | Fe-$N_{phen}$ | 2.193, 0.006Å | | Fe···plane(py) | -0.259, 0.058Å | |
| | | Fe-$N_{pz}$ | 2.160, 0.056Å | | Fe···plane(pz) | -0.451, -0.897Å | |
| | | Fe···B | 3.491, 0.036 | | | 0.386, 0.488Å | |
| | | N-Fe-$N_{phen}$ | 74.93° | | $py\hat{\cdots}py$ (phen) | 6.85(15)° | |
| | | N-Fe-$N_{pz}$ | 88.74, 3.72° | | | | |
| | | N-B-N | 109.88, 0.14° | | | | |

***Table S14.*** *Calculated Fe Electric Field Gradients eigenvalues, corresponding quadrupole splitting and asymmetry parameter.*

| Spin state | Structure | $V_{ZZ}$ (au) | $V_{XX}/V_{YY}$ (au) | Δ (mm/s) | η |
|---|---|---|---|---|---|
| Singlet | X-ray 100 K($C_1$) | 0.1534 | -0.0038/-0.1495 | 0.283(18) | 0.9499 |
| | Optimized ($C_1$) | 0.1264 | -0.0215/-0.1049 | 0.219(14) | 0.6598 |
| Quintet | X-ray 200 K ($C_2$) | -1.8263 | 0.9059/0.9204 | 2.96(18) | 0.0080 |
| | Optimized ($C_1$) | -2.1021 | 1.0341/1.0680 | 3.40(21) | 0.0161 |
| | X-ray 30 K ($C_1$) | -2.0361 | 0.8699/1.1662 | 3.31(21) | 0.1455 |

## References

1 S. Rat, M. Mikolasek, J. S. Costá, A. I. Chumakov, W. Nicolazzi, G. Molnár, L. Salmon and A. Bousseksou, *Chem. Phys. Lett.*, 2016, **653**, 131–136.

2 A. Pronschinske, R. C. Bruce, G. Lewis, Y. Chen, A. Calzolari, M. Buongiorno-Nardelli, D. A. Shultz, W. You and D. B. Dougherty, *Chem. Commun.*, 2013, **49**, 10446.

3 L. Kipgen, M. Bernien, S. Ossinger, F. Nickel, A. J. Britton, L. M. Arruda, H. Naggert, C. Luo, C. Lotze, H. Ryll, F. Radu, E. Schierle, E. Weschke, F. Tuczek and W. Kuch, *Nat. Commun.*, 2018, **9**, 1–8.

4 Gaussian 16, M. J. Frisch, G. W. Trucks, H. B. Schlegel, G. E. Scuseria, M. A. Robb, J. R. Cheeseman, G. Scalmani, V. Barone, G. A. Petersson, H. Nakatsuji, X. Li, M. Caricato, A. V. Marenich, J. Bloino, B. G. Janesko, R. Gomperts, B. Mennucci, H. P. Hratchian, J. V. Ortiz, A. F. Izmaylov, J. L. Sonnenberg, D. Williams-Young, F. Ding, F. Lipparini, F. Egidi, J. Goings, B. Peng, A. Petrone, T. Henderson, D. Ranasinghe, V. G. Zakrzewski, J. Gao, N. Rega, G. Zheng, W. Liang, M. Hada, M. Ehara, K. Toyota, R. Fukuda, J. Hasegawa, M. Ishida, T. Nakajima, Y. Honda, O. Kitao, H. Nakai, T. Vreven, K. Throssell, J. A. Montgomery, Jr., J. E. Peralta, F. Ogliaro, M. J. Bearpark, J. J. Heyd, E. N. Brothers, K. N. Kudin, V. N. Staroverov, T. A. Keith, R. Kobayashi, J. Normand, K. Raghavachari, A. P. Rendell, J. C. Burant, S. S. Iyengar, J. Tomasi, M. Cossi, J. M. Millam, M. Klene, C. Adamo, R. Cammi, J. W. Ochterski, R. L. Martin, K. Morokuma, O. Farkas, J. B. Foresman, and D. J. Fox, Gaussian, Inc., Wallingford CT, 2016.

5 A. L. Thompson, A. E. Goeta, J. A. Real, A. Galet and M. Carmen Muñoz, *Chem. Commun.*, 2004, **12**, 1390–1391.

6 F. Remacle, F. Grandjean and G. J. Long, *Inorg. Chem.*, 2008, **47**, 4005–4014.

7 H. Paulsen and A. X. Trautwein, *Top. Curr. Chem.*, 2004, **235**, 197–219.

8 A. D. Bochevarov, R. A. Friesner and S. J. Lippard, *J. Chem. Theory Comput.*, 2010, **6**, 3735–3749.